ТЕСЛИНИ ИНОВАЦИОНИ ДАНИ
TESLA INNOVATION DAYS
Belgrade, Serbia, April 7 - 8, 2025

PROCEEDINGS

Advances in Electromagnetic Coupling Applications and Protection

Organizer

NIKOLA TESLA INSTITUTE

NIKOLA TESLA INSTITUTE OF ELECTRICAL ENGINEERING

Endorsements

Ministry of Science, Technological Development and Innovation of the Republic of Serbia

Science Fund of the Republic of Serbia

Sponsors

THE WORLD BANK
IBRD • IDA | WORLD BANK GROUP

#ЕУ ЗА ТЕБЕ

Technical organizer

BBN
CONGRESS MANAGEMENT
OSNOVANO / FOUNDED IN 1989

PUBLISHED BY
Nikola Tesla Institute of Electrical Engineering, University of Belgrade
Koste Glavinića 8a, 11040 Belgrade, Serbia, PO Box 139
+381 (0)11 39-52-000 | +381 (0)11 36-90-823 | +381 (0)11 36-90-487
info@ieent.org | https://www.ieent.org/

EDITOR
Dr. Maja Grbić

TECHNICAL EDITOR
Tatjana Jugović-Repajić

TECHNICAL SUPPORT & COVER DESIGN
BBN Congress Management d.o.o.

PRINTED BY
GPC Grafičko poslovni centar d.o.o. Beograd

COPIES
Printed in 150 copies

PUBLISHING PLACE
Belgrade

PUBLISHING YEAR
2025

TESLA INNOVATION DAYS – TID 2025

https://teslini-inovacioni-dani.com/

DOI: 10.5937/TID25

ISBN 978-86-83349-21-0

CIP - Каталогизација у публикацији
Народна библиотека Србије, Београд

621.319(082)
537.8(082)

ТЕСЛИНИ иновациони дани (2025 ; Београд)
Advances in Electromagnetic Coupling : applications and protection : proceedings / Теслини иновациони дани, ТИД = Tesla Innovation Days, TID, Belgrade, Serbia, April 7-8, 2025 ; [editor Maja Grbić] ; [organizer Nikola Tesla Institute]. - Belgrade : University, Nikola Tesla Institute of Electrical Engineering, 2025 (Beograd : GPC Grafičko poslovni centar). - 46 str. : ilustr. ; 30 cm

Тираж 150. - Str. 6-7: Foreword / Maja Grbić, Žarko Janda. - Bibliografija uz svaki rad. - Abstracts.

ISBN 978-86-83349-21-0

a) Електромагнетско поље -- Зборници

COBISS.SR-ID 183812105

COMMITTEES

Dr. Maja Grbić, Research Associate, Nikola Tesla Institute, president of TID Conference

PROGRAM COMMITTEE

Dr. Dragan Kovačević, Principal Research Fellow, Nikola Tesla Institute
Dr. Maja Grbić, Research Associate, Nikola Tesla Institute
Zoran Manasijević, Nikola Tesla Institute
Zoran Ćirić, Nikola Tesla Institute
Aleksandar Pavlović, Nikola Tesla Institute
Mr. Velimir Unković, Nikola Tesla Institute
Dr. Jelena Lukić, Senior Research Associate, Nikola Tesla Institute
Dr. Žarko Janda, Senior Research Associate, Nikola Tesla Institute
Dr. Jasna Dragosavac, Senior Research Associate, Nikola Tesla Institute
Prof. Dr. Vladimir Terzija, Newcastle University, UK
Prof. Dr. Jovica Milanović, The University of Manchester, UK
Dr. Milan Prodanović, IMDEA Energy Institute, Spain
Prof. Dr. Aldo Canova, Politecnico di Torino, Italy
MSc. Goran Drobnjak, GE Vernova, Germany
Nenad Uzelac, G&W Electric Co., USA
Dr. Jelena Ponoćko, SP Energy Networks, UK
Prof. Dr. Jovan Mikulović, School of Electrical Engineering, University of Belgrade
Nebojša Petrović, Energy Agency of the Republic of Serbia, CIGRE Serbia
Dr. Vladimir Šiljkut, Electric Power Industry of Serbia
MSc. Dušan Vukotić, Electric Power Distribution Company of Serbia
Dr. Nikola Kuljača, CIGRE Montenegro, Montenegro
Mićo Todorović, Public Health Institute of the Republic of Srpska, Bosnia and Herzegovina

ORGANIZING COMMITTEE

Aleksandar Pavlović, Nikola Tesla Institute
Saša Milovanović, Nikola Tesla Institute
Branka Kovačević, Nikola Tesla Institute
Dr. Valentina Vasović, Research Associate, Nikola Tesla Institute
Dr. Draginja Mihajlović, Research Associate, Nikola Tesla Institute
Milica Đukić, Nikola Tesla Institute
Marjan Stojković, Nikola Tesla Institute

PAPER REVIEWERS

Dr. Maja Grbić, Research Associate, Nikola Tesla Institute
Prof. Dr. Aldo Canova, Politecnico di Torino, Italy
Prof. Dr. Adnan Mujezinović, Faculty of Electrical Engineering, University of Sarajevo, Bosnia and Herzegovina
Dr. Ajdin Alihodžić, Faculty of Electrical Engineering, University of Sarajevo, Bosnia and Herzegovina
Prof. Dr. Maja Muftić Dedović, Faculty of Electrical Engineering, University of Sarajevo, Bosnia and Herzegovina
Dr. Žarko Janda, Senior Research Associate, Nikola Tesla Institute
Dr. Uroš Radoman, Research Associate, Nikola Tesla Institute
Aleksandar Pavlović, Nikola Tesla Institute

CONTENT

FOREWORD

Advances in Electromagnetic Coupling Applications in Power Systems Engineering and Protection against Electromagnetic Fields and Interference

Introduction

The rapid evolution of the modern electrical landscape is characterized by increasingly complex interactions between electromagnetic fields and infrastructure. A lot of presented research and advances were foreseen by Nikola Tesla. As power transmission networks expand and sensitive electronic systems proliferate, the study of electromagnetic coupling—both intentional and parasitic—has become a cornerstone of ensuring system reliability, personnel safety, and operational efficiency. These proceedings bring together a collection of papers that explore the frontiers of electromagnetic phenomena, ranging from the diagnostic analysis of power transformers and the safety of high-voltage transmission line maintenance to the cutting-edge development of wireless charging and advanced shielding materials.

A central theme in these proceedings is related to electromagnetic coupling phenomena i.e. the utilization of electromagnetic signatures for diagnostic and functional purposes as well as protection of people and equipment from electromagnetic fields. In the realm of power equipment, the ability to detect internal faults without invasive procedures is paramount. Similarly, the intentional application of inductive coupling is revolutionizing the transportation sector through wireless power transfer. However, these advancements come with the challenge of managing unintended coupling, such as conductive interference between earthing grids and buried pipelines, and the necessity of protecting the general public and workers from non-ionizing radiation.

Technical Contributions and Innovations

The papers included in these proceedings address these challenges through a mix of numerical modelling, experimental validation, and material science innovation.

The engineering of power conversion and transmission is explored in **"Wireless Chargers for Electric Vehicles – Challenges and Solution".** The research on wireless chargers tackles inherent inefficiencies such as misalignment and weak magnetic coupling through auxiliary coil compensation and single-stage matrix converters, achieving 97% efficiency.

In the field of power transformer diagnostics, **"Application of the Nonlinear Kernel Principal Component Analysis in Detecting Disk-to-Disk Faults Along a Transformer Winding"** investigates the detection of short-circuit faults. By combining Frequency Response Analysis (FRA) with Nonlinear Kernel Principal Component Analysis (KPCA), the authors provide a robust framework for localizing faults within high-voltage windings. Their R–L–C–M analytical model, validated against laboratory measurements, demonstrates how dimensionality reduction can transform complex electromagnetic signatures into actionable diagnostic data.

Safety of workers and environmental impact are addressed in **"Methodology for the Assessment of Exposure of Workers to Electric and Magnetic Fields During Maintenance Work on Double-Circuit Transmission Overhead Power Lines"** and **"Analysis of Electromagnetic Field Levels in the Vicinity of the Mixed Transmission Power Line Tower at the Location of Transition from Overhead to Cable Section".** The first one confirms that during work on the passive system of a double-circuit line the field levels remain within the limits prescribed by Directive 2013/35/EU. The second one identifies that magnetic field levels are highest at transition zones between overhead and underground sections, suggesting that conductive shielding or physical barriers may be necessary to meet public safety limits for non-ionizing radiation.

The proceedings also address the mitigation of electromagnetic interference (EMI) and hazardous coupling. **"Innovation in EMI Shielding Materials Integrated in GrInShield Project – Twinning for New Graphene Based Nanomaterials"** introduces sustainable innovations, detailing the development of graphene-based composites and biochar for lightweight, eco-friendly EMI shielding. The research demonstrates that integrating metal-based nanomaterials can significantly enhance shielding effectiveness across a wide frequency range. Complementing this, **"Analysis of the Conductive Coupling Between 220/66/11 kV Substation and Nearby Pipeline During Earth Fault"** provides a critical analysis of conductive interference. It highlights the risks of high touch voltages during earth faults and proposes specific mitigation strategies to protect personnel and infrastructure.

Finally, the paper **"Innovative Instrument Design for Systems with Varying Frequency Inputs"** presents a frequency multiplication circuit designed to eliminate spectral leakage in grids with varying frequency inputs, allowing for more efficient use of computational resources in power quality monitoring.

Emerging Trends in the Proceedings

Beyond the individual technical contributions, a synthesis of the included papers reveals several cross-cutting trends that define the current state of research in power systems and apparatus. These common features underscore the shift toward more sophisticated, data-driven, and sustainable engineering practices.

- **Integration of Computational Modelling and Experimental Validation:** A predominant feature across these works—specifically evident in the studies on transformer faults and mixed transmission lines—is the reliance on a "dual-track" methodology. Researchers are no longer relying solely on empirical measurements; instead, they develop complex numerical models (such as R–L–C–M networks or specialized field simulation software) and rigorously validate them against real-world or laboratory data. This approach ensures that the resulting diagnostic tools and safety protocols are both theoretically sound and practically applicable.
- **Nonlinear Signal Processing and Advanced Data Analytics:** As electromagnetic signatures become more complex, traditional linear analysis is being superseded. The use of Kernel Principal Component Analysis (KPCA) for fault detection and the development of specialized frequency multiplication circuits for power quality instruments reflect a broader trend: the necessity of advanced digital signal processing to extract meaningful information from high-dimensional or non-stationary electromagnetic data.
- **Emphasis on Occupational and Public Safety:** A significant portion of this volume is dedicated to the safety of general public and workers in the vicinity of power lines and facilities. Whether through the assessment of exposure of workers on double-circuit lines or the quantification of field levels at overhead-to-cable transition points, there is a clear focus on aligning industrial practices with international safety directives and recommendations (e.g. Directive 2013/35/EU and Recommendation 1999/519/EC). This highlights the industry's commitment to mitigating the biological risks associated with non-ionizing radiation.
- **Sustainability and Material Innovation:** The proceedings highlight a move toward "green EM field absorption" and sustainable applications. The development of new graphene-based nanomaterials derived from biochar from fruit-processing waste for EMI shielding and the optimization of Wireless Power Transfer (WPT) for electric vehicles demonstrate how electromagnetic research is directly contributing to the global energy transition and circular economy.
- **Practical Mitigation and Engineering Standards:** Finally, the papers consistently bridge the gap between theoretical physics and regulatory compliance. Each study concludes with concrete engineering recommendations—ranging from the application of insulating layers and conductive shields to the implementation of single-stage matrix converters—ensuring that the research provides immediate value to grid operators, manufacturers, and safety inspectors.

Future Directions

Together, these papers illustrate the dual nature of electromagnetic coupling in modern engineering: as a powerful tool for energy transfer, equipment fault diagnostics and as a complex challenge requiring sophisticated shielding and safety protocols. The integration of nonlinear signal processing, advanced material science, rigorous numerical modelling and new measurement protocols remains essential for the continued development of a resilient and safe power infrastructure.

Dr. Maja Grbić
Dr. Žarko Janda

ORAL PRESENTATIONS – INVITED LECTURES

ТЕСЛИНИ ИНОВАЦИОНИ ДАНИ
TESLA INNOVATION DAYS
Belgrade, Serbia, April 7 - 8, 2025

DOI: 10.5937/TID25009M

WIRELESS CHARGERS FOR ELECTRIC VEHICLES – CHALLENGES AND SOLUTION

***Nikola Mirković*[1]**

[1]*Nikola Tesla Institute of Electrical Engineering, Serbia*

nikola.mirkovic@ieent.org

Abstract

Wireless charging of electric vehicles (EVs) has emerged as a promising solution to improve user convenience and enable seamless integration of EVs into smart grids. However, several challenges hinder its widespread adoption, including low efficiency due to weak magnetic coupling, bulky multi-stage converter topologies, grid compliance issues, and misalignment between transmitter and receiver coils. This paper presents advanced solutions to address these challenges. First, a high-power bidirectional inductive charger employing an auxiliary coil with S-S-S compensation is introduced, achieving high efficiency and seamless control across alignment tolerances. Second, a single-stage charger based on a Three-phase to Single-phase Matrix Converter (TSMC) is proposed, with a novel modulation strategy that ensures constant power flow, high power factor, and low total harmonic distortion (THD) without requiring communication between controllers. Third, a compact three-phase inductive charger using DD^{2}Q coil topology and Reduced TSMC (RTSMC) converters is presented, enabling high power density and robust misalignment control. Experimental prototypes ranging from 3.3 kW to 30 kW validate the proposed concepts, achieving efficiencies up to 97% and demonstrating compliance with international standards. These innovations provide practical pathways toward efficient, reliable, and grid-compliant wireless EV charging systems.

Keywords: Wireless charging, electric vehicles, inductive power transfer, matrix converter, DD^{2}Q coil, bidirectional charger.

1 Introduction

The electrification of transportation is one of the most significant technological transitions of the 21st century. Electric vehicles (EVs) are increasingly adopted worldwide as governments and industry aim to reduce greenhouse gas emissions and dependence on fossil fuels. However, charging infrastructure remains a critical bottleneck. Conventional plug-in chargers require heavy-duty cables and user interaction, limiting convenience and scalability.

Wireless charging, based on inductive power transfer (IPT), offers a contactless alternative that enhances user experience and enables advanced functionalities such as vehicle-to-grid (V2G) energy exchange [1] – [4]. By eliminating cables, IPT systems improve safety, reliability, and user acceptance. Moreover, bidirectional wireless chargers transform EVs into distributed energy storage units, supporting microgrids and renewable integration [5], [6].

Despite these advantages, IPT systems face several challenges:

1) Low efficiency: Weak magnetic coupling and high reactive power reduce transfer efficiency [7].
2) Bulky multi-stage converters: Traditional rectifier–inverter–DC/DC chains reduce power density and increase cost [3].
3) Grid compliance: Achieving high power factor and low harmonic distortion while maintaining soft switching is challenging [8].
4) Misalignment sensitivity: Misalignment degrades coupling and power, thus improving tolerance is essential [9], [10].
5) Bidirectionality without communication: Stable power control and phase synchronization must be achieved without a live data link [11], [12].

These challenges of the IPT technology are best reflected through the requirement for compensation of the inductive link and the question of converter topology choice for energizing the entire structure. Compensation of the inductive link, that is depicted in Figure 1, is essential due to low coupling under practical geometries, alignment and clearances [7]. Most common compensation structures that can be encountered in the literature are given here:

1) Series–Series (S-S) compensation: It is simple and widely used, while its classic design guidance is well established [13]. It is given in Figure 2a.
2) Double-sided LCC compensation: Depicted in Figure 2b, it adds degrees of freedom for efficiency and tolerance and it is widely adopted in EV WPT [14].

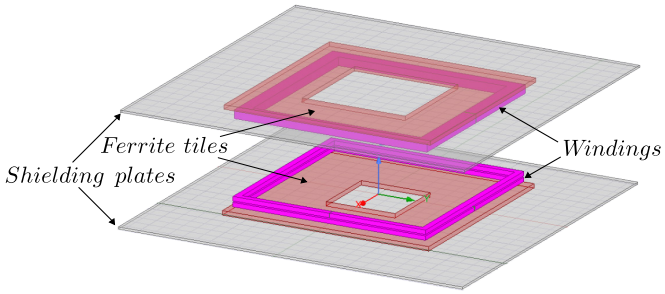

Figure 1. Typical depiction of the inductive link

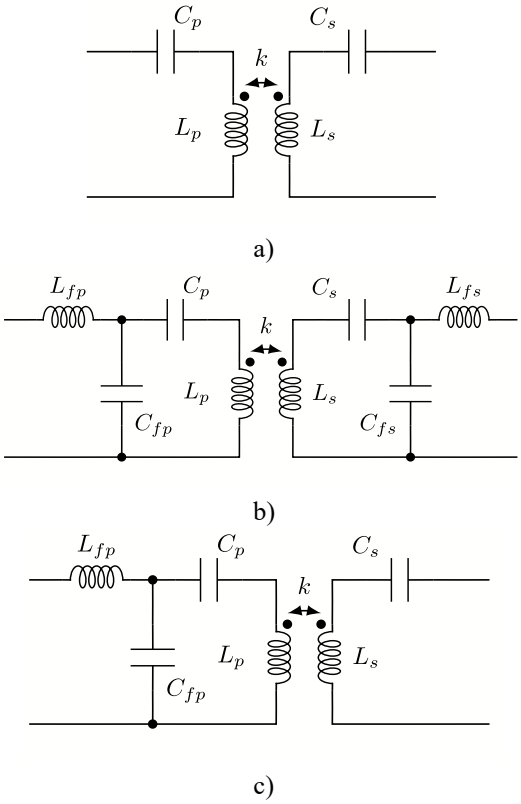

Figure 2. Common compensation strategies of the inductive link a) S-S, b) double-sided LCC, c) LCC-S

3) Hybrid LCC-S strategies: Offers CV behavior and robustness under coupling variation [15]. It is shown in Figure 2c.
4) Multi-coil links: Three-coil systems improve efficiency and enable CC/CV behavior [16]; four-coil systems are effective for specific power and geometry constraints [17].

Regarding the converter choice and number of power conversion stages, conventional IPT chargers use multiple conversion stages as it is shown in Figure 3. The single-stage approaches, that are becoming increasingly more present, shrink volume and loss. Following approaches stood out as possible attractive solutions for this technology challenge:

1) Matrix converters (TSMC and variants): Eliminate DC links and directly synthesize HF excitation from the grid [18], [19]; single-phase active-clamped variants are promising [20]. Advanced modulation improves PF and efficiency [8].

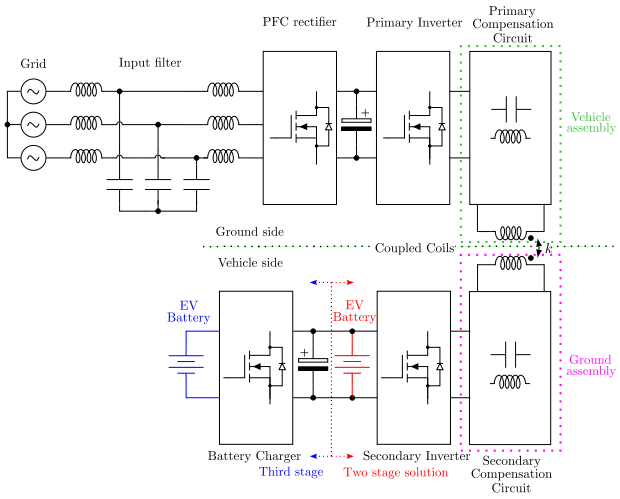

Figure 3. Structure of a traditional multi-stage EV charger

2) Alternative single-stage topologies: Unfolder–T-type AC-DC converters [21] and SWISS-DAB-based approaches [22] reduce component count while targeting bidirectionality and compliance.

Recent trends show that there is increased interest in poly-phase IPT chargers. High-power IPT benefits from poly-phase links for compactness and field shaping. Various approaches are present in articles addressing this topic:

1) Three-phase IPT converters: Oak Ridge AC/DC concepts for wireless EV charging [23].
2) Integrated three-phase AC-DC IPT with active PFC using three transmitters [24].
3) Coil topology for compactness: DD^{2}Q structures provide decoupling and high coupling, enabling compact three-phase pads [25].

2 Auxiliary coil compensation

Conventional two-coil, series–series compensated IPT systems exhibit a steep efficiency drop and unstable regulation when the coupling coefficient degrades due to air-gap and misalignment. The root cause is the rise of circulating reactive current in the tank, which amplifies copper and core losses and narrows the soft-switching window at the inverter. To address these limits, the system can be extended with an auxiliary coil placed between the transmitter and receiver as given in the Figure 4, forming a three-coil S-S-S topology together with three serial compensation capacitors. The auxiliary coil is magnetically coupled to both sides and tuned to resonate at the operating frequency, shaping the reflected impedance to the primary so that active power transfer is favored while reactive exchange is reduced. Practically, this yields higher efficiency near nominal alignment and preserves performance under lateral and angular displacement. The very idea of having an auxiliary coil is present throughout the literature. However, the main distinction of this proposal [26], is the obtained functionality of the entire charger. Namely, with the employed compensation technique and its adequate tuning, entire resonant circuit can be represented using an equivalent inductance as it is shown in Figure 5. In this way, elegant possibility for bidirectional power flow is achieved via phase-shift control.

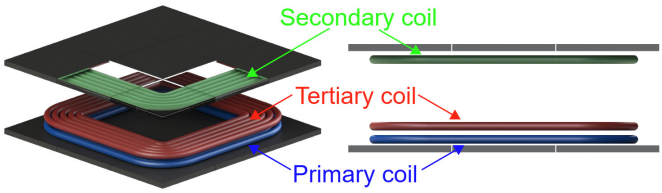

Figure 4. Proposed three coil system

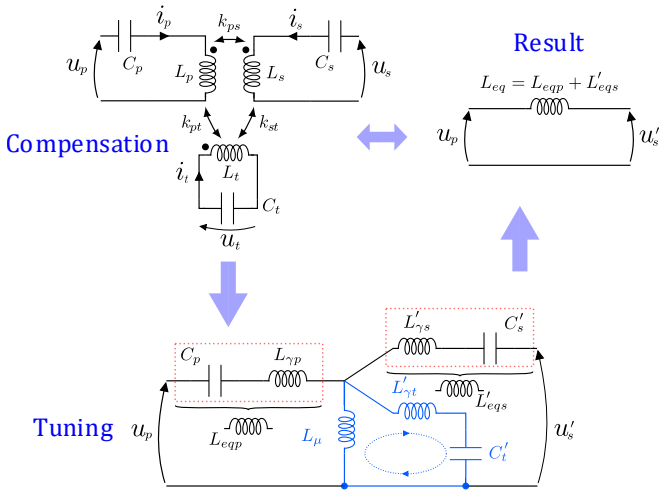

Figure 5. Tuning of the proposed compensation with auxiliary coil

The topology is constructed with three series-compensated branches: primary, auxiliary, and secondary. The design starts from the target power, frequency, and pad geometry constraints. Mutual inductances between coil pairs are obtained via electromagnetic modeling and verified with bench measurements. Using these couplings, compensation capacitors are selected to achieve desired equivalent inductance value at the operating frequency. A key outcome of the three-coil arrangement is the ability to realize constant-current or constant-voltage behavior by a simple control algorithm, regulating the power flow via phase-shift. Coil geometry is optimized to maximize useful coupling and minimize stray fields, including the choice of Litz wire strand count, ferrite plate thickness, and spacing. Entire design procedure is detailly explained in [26]. Shielding and spacing are chosen to reduce eddy losses and keep leakage within safety margins.

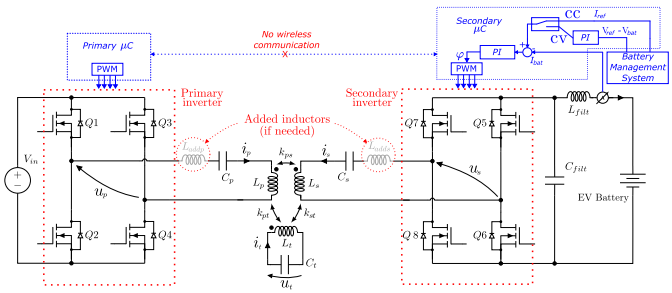

Figure 6. Charger topology

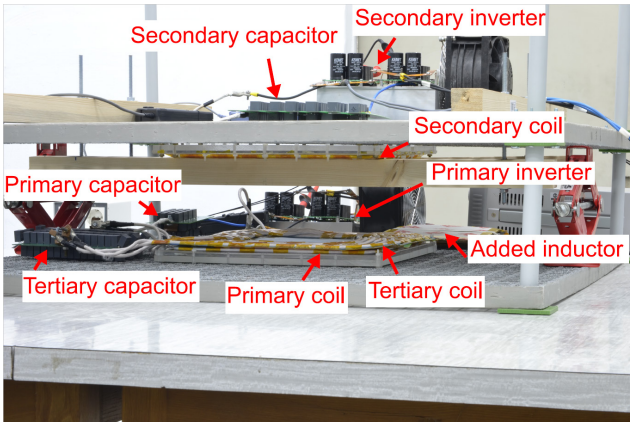

Figure 7. Constructed 30 kW prototype of the proposed IPT charger

Converter considered in this case is given in Figure 6, having only the DC/DC resonant stage. Control of the primary inverter is kept simple: a fixed-frequency, square-wave excitation with a modulation that maintains high efficiency of the system, adjusting the duty cycle based on system operating conditions. Because the auxiliary branch reduces the reactive power that is coming from the inverters, their currents are lower for the same transferred power, enhancing the power transfer capability and easing device stress. On the secondary, rectification and output filtering are dimensioned to meet CC/CV charging requirements without oscillation or excessive ripple. The system is validated across load variation and displacement ranges representative of EV parking tolerances. Measurement protocols include total efficiency, secondary regulation accuracy, and thermal steady-state at full load. Uncertainty is reduced by repeated runs and warm-up prior to data capture.

Experimental results obtained on a 30 kW prototype that was designed and constructed and that is shown in Figure 7, demonstrate that the auxiliary-coil topology sustains high efficiency at nominal alignment and maintains performance under misalignment. Efficiency remains above typical two-coil baselines when the coupling coefficient drops due to lateral displacement, and reactive power is measurably lower in the primary tank for equivalent output. The CC/CV transition is smooth, with no need for fast communication between controllers. This is also pointed out on Figure 6, emphasizing one of the advantages of this compensation – no wireless communication between primary and secondary microcontrollers is required for this system to operate. The approach scales with coil area and frequency, making it applicable from low-power pads to high power chargers, provided the auxiliary coil is proportionally tuned and shielded. Compared against the two-coil reference, the proposed system shows superior robustness to misalignment, improved efficiency at reduced coupling, and simpler regulation for EV charging profiles.

3 Single-stage EV charger based on TSMC

Conventional IPT chargers are typically realized with multiple conversion stages as shown in Figure 3: an AC/DC rectifier with a bulky DC link, a high-frequency DC/DC resonant stage incorporating the inductive link, and often an

additional DC/DC stage for regulation. While effective, this architecture increases losses, size, and cost. To overcome these drawbacks, a single-stage charger solution based on a Three-Phase to Single-Phase Matrix Converter, incorporating the previously described inductive link compensation with auxiliary coil, was developed in [27] and it is given in Figure 8. The matrix converter directly synthesizes the high-frequency excitation required for the inductive link from the three-phase grid, eliminating the bulky DC link and reducing passive component count.

The proposed topology employs bidirectional switches arranged to perform direct AC-AC conversion. By appropriate modulation, the converter generates a sinusoidal current at the resonant frequency of the IPT coils while simultaneously shaping the input currents to achieve unity power factor. This is the first big innovation in this work – a novel modulation strategy for the TSMC. The modulation strategy was designed to ensure constant power transfer and low harmonic distortion, while also enabling soft-start capability to avoid inrush currents.

Second key innovation of this work is the communication-free synchronization between the primary and secondary sides. Instead of relying on a data link, synchronization is achieved through the inherent properties of the resonant link and modulation scheme. This reduces system complexity and enhances reliability, particularly in automotive environments where communication can be unreliable.

The design process begins with analytical modelling of the converter switching states and their impact on both input and output waveforms. Simulation studies confirmed that the proposed modulation achieves sinusoidal input currents with total harmonic distortion below 5% and maintains stable output power across load variations. The hardware prototype was implemented with high-frequency SiC MOSFETs and optimized gate drivers to minimize switching losses.

Experimental validation was carried out on a 3.3 kW prototype that is shown in Figure 9. Results demonstrated efficiency above 95% at nominal operating conditions, with input current THD below 5% and displacement power factor close to unity. The charger operated stably across a wide range of load conditions and tolerated misalignment without loss of regulation. The absence of a DC link capacitor significantly reduced system volume and improved power density, making the topology attractive for EV applications.

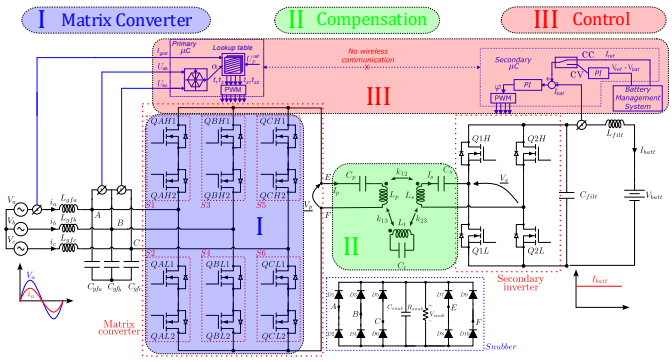

Figure 8. Topology of the proposed single-stage IPT charger

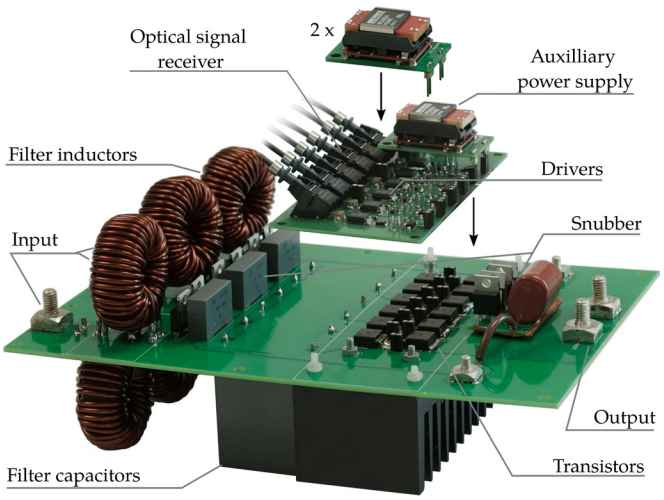

Figure 9. A 3.3 kW prototype of the employed TSMC

This work shows that matrix-converter-based single-stage IPT chargers can achieve high efficiency, compact design, and compliance with grid standards, while simplifying control and reducing component count. The complete theoretical derivation, modulation strategy, and experimental results are presented in [27].

4 Three-phase, single-stage charger based od DD2Q coil topology

High-power wireless charging systems require coil structures and converter architectures that can sustain high power transfer, while remaining compact and tolerant to misalignment. Conventional two-coil systems are limited by poor coupling at large air gaps, while multi-stage converters reduce efficiency and power density. To address these challenges, a three-phase, single-stage IPT charger was developed in [28], combining a DD^{2}Q coil topology with a four-switch, direct matrix-converter-based AC–AC stage.

The DD^{2}Q coil topology that is shown in Figure 10, was chosen because it provides mutual decoupling between phases, high effective coupling coefficients, and compact geometry. By properly constructing and aligning the coils, phase decoupling is achieved, as well as balanced flux distribution, which is critical for stable three-phase operation. This structure allows higher power transfer capability while reducing current stress per coil, thereby improving thermal performance and robustness under misalignment.

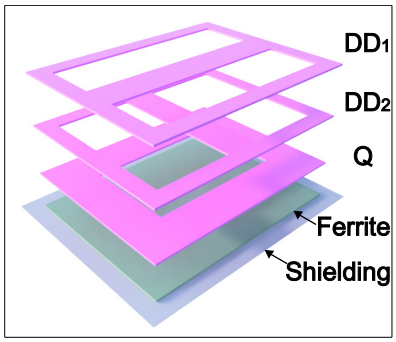

Figure 10. DD2Q coil topology

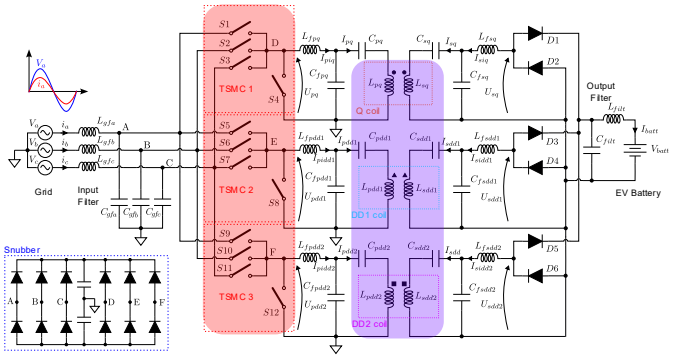

Figure 11. Topology of the proposed three-phase, single-stage charger

On the converter side, the bulky DC link is eliminated as the consequence of using a matrix converter topology. Entire system structure is shown in Figure 11. A Reduced Three-phase to Single-phase Matrix Converter directly synthesizes the high-frequency excitation required by the IPT link while shaping input currents for near-unity power factor. This employed modulation ensures compliance with grid standards and reduces harmonic distortion without additional filtering. Importantly, besides the modulation, a balancing algorithm is proposed, solving the phase disbalance in power distribution under misalignment conditions, maintaining balanced secondary currents even under misalignment between ground and vehicle assemblies, preventing saturation and ensuring stable operation.

The design methodology included electromagnetic modelling of the DD^{2}Q coil system, optimization of compensation networks for resonance at 85 kHz, and analytical derivation of the reduced modulation strategy. Simulation studies confirmed sinusoidal input currents with low THD and stable output power across a wide range of coupling coefficients.

A 24 kW prototype that is shown in Figures 12a and 12b was constructed to validate the concept. Measurements showed end-to-end efficiency below 90% at nominal alignment, reflecting the combined impact of conduction and switching losses, and demonstrating misalignment tolerance requirements. Despite this, the system maintained balanced currents, stable power delivery under ±100 mm lateral misalignment, and acceptable thermal performance. Grid current quality met the intended targets, demonstrating the feasibility of single-stage three-phase IPT at this power level.

This chapter demonstrates that the combination of DD^{2}Q coil topology and RTSMC enables a compact, robust three-phase IPT charger suitable for high-power EV applications. While efficiency remains a challenge at 24 kW, the architecture proves that poly-phase wireless charging can be realized in a single stage, paving the way for further optimization in coil design, device selection, and modulation strategies. The complete derivations, design rules, and experimental campaign are documented in [28].

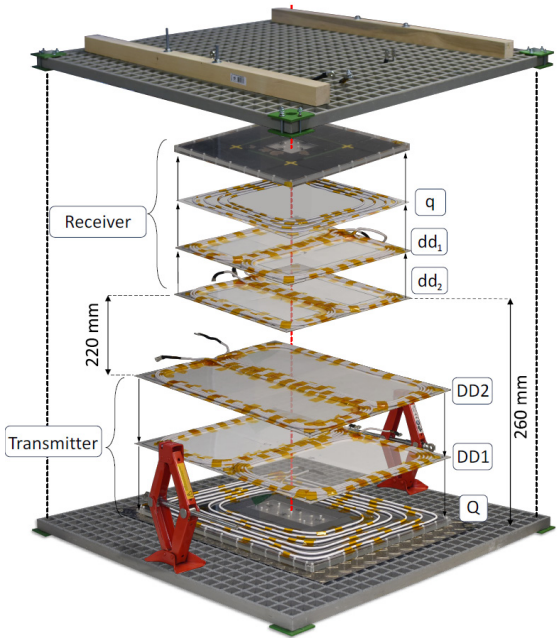

a)

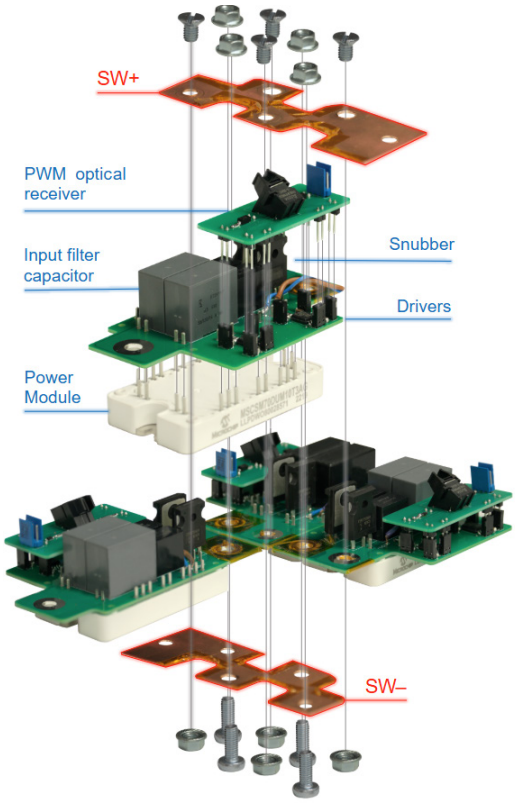

b)

Figure 12. a) Prototype of the DD2Q coil topology, b) RTSMC prototype

5 Conclusions

Wireless charging of electric vehicles continues to face several barriers to widespread adoption. The most critical challenges include efficiency losses at high power, bulky and costly multi-stage converter architectures, difficulty in meeting grid compliance standards, and sensitivity to misalignment between coils. These issues limit reliability, increase system cost, and slow down the transition from laboratory prototypes to commercial deployment.

This work points out to the three recently proposed solutions that directly tackle these obstacles:

- Auxiliary coil compensation reduces reactive power and improves efficiency, while enhancing tolerance to misalignment. It also allows for seamless control that is independent on real-time wireless communication.
- Single-stage matrix-converter charger eliminates the DC link, simplifying the architecture and improving grid compliance with high efficiency.
- Three-phase DD^2Q coil charger scales wireless charging to higher power levels, maintaining balanced operation and robustness under displacement.

Together, these approaches demonstrate practical pathways to overcome the main limitations of IPT systems. By addressing efficiency, compactness, compliance, and misalignment tolerance, they provide strategies that can accelerate the adoption of wireless charging technology in real EV applications. The proposed topologies show how targeted innovations can bridge the gap between current limitations and the requirements of widespread deployment.

6 References

[1] R. Tavakoli, Z. Pantic, "Analysis, Design, and Demonstration of a 25-kW Dynamic Wireless Charging System for Roadway Electric Vehicles," IEEE J. Emerg. Sel. Topics Power Electron., 6(3), 1378–1393, 2018. doi: 10.1109/JESTPE.2017.2761763.

[2] H. Wang, U. Pratik, A. Jovicic, et al., "Dynamic Wireless Charging of Medium Power and Speed Electric Vehicles," IEEE Trans. Veh. Technol., 70(12), 12552–12566, 2021. doi: 10.1109/TVT.2021.3122366.

[3] S. Li, C. C. Mi, "Wireless Power Transfer for Electric Vehicle Applications," IEEE J. Emerg. Sel. Topics Power Electron., 3(1), 4–17, 2015. doi: 10.1109/JESTPE.2014.2319453.

[4] D. Patil, M. K. McDonough, J. M. Miller, et al., "Wireless Power Transfer for Vehicular Applications: Overview and Challenges," IEEE Trans. Transport. Electrific., 4(1), 3–37, 2018. doi: 10.1109/TTE.2017.2780627.

[5] S. Lukic, Z. Pantic, "Cutting the Cord: Static and Dynamic Inductive Wireless Charging of Electric Vehicles," IEEE Electrification Mag., 1(1), 57–64, 2013. doi: 10.1109/MELE.2013.2273228.

[6] Z. Pantic, S. Bai, S. M. Lukic, "Inductively Coupled Power Transfer for Continuously Powered Electric Vehicles," Proc. IEEE VPPC, 1271–1278, 2009. doi: 10.1109/VPPC.2009.5289705.

[7] R. Bosshard, J. W. Kolar, "Multi-Objective Optimization of 50 kW/85 kHz IPT System for Public Transport," IEEE J. Emerg. Sel. Topics Power Electron., 4(4), 1370–1382, 2016. doi: 10.1109/JESTPE.2016.2598755.

[8] L. Schrittwieser, M. Leibl, J. W. Kolar, "99% Efficient Isolated Three-Phase Matrix-Type DAB Buck-Boost PFC Rectifier," IEEE Trans. Power Electron., 35(1), 138–157, 2020. doi: 10.1109/TPEL.2019.2914488.

[9] F. Yang, Y. Liu, Y. Han, et al., "Misalignment Tolerance Improvement for Loosely Coupled Transformer of IPT Systems via an Intermediate Coil with Detuned Compensation," IEEE Access, 11, 90181–90189, 2023. doi: 10.1109/ACCESS.2023.3306955.

[10] N. Mirkovic, A. Delgado, P. Alou, et al., "Increasing Power Transfer Capability of Wireless Battery Charger Under Misalignment Conditions," PCIM Europe 2023, 1–8, 2023. doi: 10.30420/566091236.

[11] F. Liu, K. Li, K. Chen, et al., "A Phase Synchronization Technique Based on Perturbation and Observation for Bidirectional Wireless Power Transfer System," IEEE J. Emerg. Sel. Topics Power Electron., 8(2), 1287–1297, 2020. doi: 10.1109/JESTPE.2019.2942101.

[12] T. Tan, K. Chen, Y. Jiang, et al., "A Bidirectional Wireless Power Transfer System Control Strategy Independent of Real-Time Wireless Communication," IEEE Trans. Ind. Appl., 56(2), 1587–1598, 2020. doi: 10.1109/TIA.2019.2961311.

[13] C.-S. Wang, O. H. Stielau, G. A. Covic, "Design Considerations for a Contactless Electric Vehicle Battery Charger," IEEE Trans. Ind. Electron., 52(5), 1308–1314, 2005. doi: 10.1109/TIE.2005.855672.

[14] S. Li, W. Li, J. Deng, et al., "A Double-Sided LCC Compensation Network and Its Tuning Method for Wireless Power Transfer," IEEE Trans. Veh. Technol., 64(6), 2261–2273, 2015. doi: 10.1109/TVT.2014.2347006.

[15] I.-W. Iam, C.-K. Choi, C.-S. Lam, et al., "A Constant-Power and Optimal-Transfer-Efficiency Wireless Inductive Power Transfer Converter for Battery Charger," IEEE Trans. Ind. Electron., 71(1), 450–461, 2024. doi: 10.1109/TIE.2023.3241408.

[16] W. X. Zhong, C. Zhang, X. Liu, et al., "A Methodology for Making a Three-Coil Wireless Power Transfer System More Energy Efficient Than a Two-Coil Counterpart," IEEE Trans. Power Electron., 30(2), 933–942, 2015. doi: 10.1109/TPEL.2014.2312020.

[17] Y. Zhang, Z. Zhao, T. Lu, "Quantitative Analysis of System Efficiency and Output Power of Four-Coil Resonant Wireless Power Transfer," IEEE J. Emerg. Sel. Topics Power Electron., 3(1), 184–190, 2015. doi: 10.1109/JESTPE.2014.2319295.

[18] N. X. Bac, D. M. Vilathgamuwa, U. K. Madawala, "A SiC-Based Matrix Converter Topology for Inductive Power Transfer System," IEEE Trans. Power Electron., 29(8), 4029–4038, 2014. doi: 10.1109/TPEL.2013.2291434.

[19] L. Guan, Z. Wang, P. Liu, et al., "A Three-Phase to Single-Phase Matrix Converter for Bidirectional Wireless

Power Transfer System," IECON 2019, 4451–4456, 2019. doi: 10.1109/IECON.2019.8927585.

[20] P. S. Huynh, D. Ronanki, D. Vincent, et al., "Direct AC-AC Active-Clamped Half-Bridge Converter for Inductive Charging Applications," IEEE Trans. Power Electron., 36(2), 1356–1365, 2021. doi: 10.1109/TPEL.2020.3009395.

[21] A. Zade, C. R. Teeneti, M. Mansour, et al., "A 21-kW Unfolding-Based Single-Stage AC-DC Converter for Wireless Charging Applications," IEEE J. Emerg. Sel. Topics Power Electron., 12(1), 8–27, 2024. doi: 10.1109/JESTPE.2023.3309588.

[22] C. S. Wong, J. Liu, L. Cao, et al., "A SWISS-Rectifier-Based Single-Stage Three-Phase Bidirectional AC-DC Inductive-Power-Transfer Converter for Vehicle-to-Grid Applications," IEEE Trans. Power Electron., 38(3), 4152–4166, 2023. doi: 10.1109/TPEL.2022.3220327.

[23] E. Asa, O. C. Onar, V. P. Galigekere, et al., "A Novel Three-Phase Oak Ridge AC/DC Converter for Wireless EV Charger Applications," APEC 2021, 437–443, 2021. doi: 10.1109/APEC42165.2021.9487063.

[24] J. Liu, C. S. Wong, Z. Li, et al., "An Integrated Three-Phase AC-DC Wireless-Power-Transfer Converter with Active Power Factor Correction Using Three Transmitter Coils," IEEE Trans. Power Electron., 38(6), 7821–7835, 2023. doi: 10.1109/TPEL.2023.3238877.

[25] B. J. Varghese, A. Kamineni, R. A. Zane, "Investigation of a DD2Q Pad Structure for High Power Inductive Power Transfer," IEEE PELS WoW 2019, 129–133, 2019. doi: 10.1109/WOW45936.2019.903064

[26] N. Mirković, L. R. Chamorro, A. Delgado, P. Alou and M. Vasić, "30 kW Bidirectional Inductive Power Transfer Charger with Intermediate Coil for EV Applications," in IEEE Transactions on Power Electronics, vol. 39, no. 7, pp. 9007-9024, July 2024, doi: 10.1109/TPEL.2024.3389129.

[27] N. R. Mirković, Đ. M. Stojić, A. Delgado, P. Alou and M. Vasić, "Novel Three-Phase to Single-Phase Matrix Converter Modulation Strategy for Bidirectional Inductive Power Transfer," in *IEEE Transactions on Power Electronics*, vol. 38, no. 12, pp. 14830-14846, Dec. 2023, doi: 10.1109/TPEL.2023.3309875.

[28] N. Mirković, A. Delgado, P. Alou and M. Vasić, "24 kW Single-Stage Three-Phase Inductive Power Transfer Charger for EV Applications Based on Matrix Converter and DD2Q Coil Topology," in *IEEE Transactions on Power Electronics*, vol. 41, no. 2, pp. 2991-3010, Feb. 2026, doi: 10.1109/TPEL.2025.3609213.

ТЕСЛИНИ ИНОВАЦИОНИ ДАНИ
TESLA INNOVATION DAYS
Belgrade, Serbia, April 7 - 8, 2025

DOI: 10.5937/TID25016R

APPLICATION OF THE NONLINEAR KERNEL PRINCIPAL COMPONENT ANALYSIS IN DETECTING DISK-TO-DISK FAULTS ALONG A TRANSFORMER WINDING

Ebrahim Rahimpour[1*], Mohammed Bilal Ghorbal [2], Hassan Reza Mirzaei[2]

[1]Technical University of Applied Sciences Würzburg-Schweinfurt, Schweinfurt, Germany
[2]Department of Electrical Engineering, University of Zanjan, Zanjan, Iran

Abstract

Rapid and accurate identification of short-circuit (SC) faults in transformer windings is essential to ensure power system reliability and reduce the need for extensive, costly laboratory testing. Since SC faults often originate from transient overvoltages in the grid, reliable diagnostic techniques are required to determine both their location and severity. Among these techniques, the Frequency Response Analysis (FRA) method is widely recognized for its effectiveness in detecting electrical faults in transformer windings under controlled High-Voltage (HV) laboratory conditions. This paper investigates an HV, single, specially fabricated disc winding and measures its Frequency Responses (FRs) under both healthy and disc-to-disc SC conditions using the FRA method. A detailed electrical model of the winding is then developed using analytical expressions. Various SC scenarios are systematically introduced into the model, and the corresponding FRs are simulated. The simulated results are validated against measured FRs, confirming the accuracy of the modeling approach. To further enhance fault characterization, Kernel Principal Component Analysis (KPCA) is applied to the simulated FRs to extract salient features and cluster them in a low-dimensional space based on fault location. The findings demonstrate the potential of combining FRA-based measurements, detailed modelling, and nonlinear feature extraction as a foundational step toward reliable SC fault detection in practical transformer windings.

Keywords: Disc-to-Disc Fault, short circuit detection, low voltage impulse method, feature extraction.

1 Introduction

Transient overvoltages in power networks can impose severe electrical stresses on transformer winding insulation. In disc-type windings, these stresses are distributed unevenly across the insulation spacers between adjacent discs. When the electric stress across a disc-to-disc insulation exceeds its dielectric strength, breakdown occurs, resulting in a Short-Circuit (SC) or Disc-to-Disc Fault (DDF). According to [1], approximately 30% of transformer failures are associated with winding-related faults. Therefore, detecting and accurately diagnosing such faults, followed by timely maintenance, are essential to prevent high SC currents from propagating through the winding and triggering further damage. This, in turn, extends transformer service life, enhances power system reliability, and reduces the likelihood of widespread outages.

A variety of monitoring techniques are available for assessing transformer health, including dissolved gas-in-oil analysis and thermal monitoring based on load current and temperature [2]. Moreover, Frequency Response Analysis (FRA) is among the most widely used techniques for identifying both electrical and mechanical defects in transformer windings [3]. Using FRA, numerous studies have focused on distinguishing DDFs from mechanical deformation faults, including axial displacement, radial deformation, and disc-spacing variations [3, 4]. In [4], a comparison index, referred to as the windowed calculation index, was introduced to compute numerical indicators from each Frequency Response (FR). These indicators were then processed using Fisher Discriminant Analysis (FDA), a linear dimensionality reduction method, to extract features for fault classification. Additionally, the authors in [3] employed vector fitting to estimate the polynomial and real coefficients of rational functions representing the FRs of the test winding. These coefficients were subsequently used as inputs to a probabilistic neural network to classify multiple fault types. Further, in [5], statistical control charts were utilized to interpret FRA results and improve discrimination between electrical and mechanical faults. Mathematical tools such as cross-correlation and standard deviation have also been explored to compute essential features for training multilayer perceptrons to identify winding fault types [6].

Other studies have investigated Artificial Neural Network (ANN)-based approaches to determine the location and severity of DDFs in various transformer windings [7]. In [8], only measured FRs obtained from healthy and faulty windings were directly fed into a Support Vector Regression (SVR)

model to estimate the fault location. Deep learning techniques have also been explored; for example, Convolutional Neural Networks (CNNs) have been applied to classify DDFs in distribution transformer windings using image-based representations of FRs [9]. Moreover, statistical indices remain a powerful tool for quantifying FR similarity and determining DDF locations [10].

Despite these advancements, many existing techniques rely on linear feature extraction methods or predefined statistical indicators, which may not fully capture the nonlinear behavior of FR variations under electrical fault conditions. To address this limitation, the present study investigates the effectiveness of Kernel Principal Component Analysis (KPCA), a nonlinear dimensionality reduction technique, in extracting and clustering features from FRs of a single High-Voltage (HV) disc winding under intact and SC conditions. The capability of KPCA to reveal distinct low-dimensional clusters corresponding to different fault locations is also evaluated.

The remainder of this paper is organized as follows. Section 2 describes the modeling methodology for the test winding. Section 3 validates the developed model by comparing simulated and experimentally measured FRs. Section 4 describes the KPCA algorithm. Section 5 illustrates the detection of DDFs in the test winding. Finally, Section 6 summarizes the key findings and contributions of this study.

2 Modeling of the HV winding

The detailed model, including all R-L-C-M elements, is widely recognized as an appropriate representation for studying electrical faults in disc-type transformer windings over a frequency range up to 1 MHz [3]. The test winding used in this study is illustrated in Fig. 1(a), and its geometric dimensions are provided in Fig. 1(b). The winding consists of 60 discs, each comprising 9 turns. In the modeling process, every two consecutive discs are grouped into a single unit, resulting in 30 units in the detailed model shown in Fig. 2.

Each model unit is represented by a set of R-L-C-M elements. The series resistance, R_{Si}, accounts for conductor (copper) losses, while R_{Pi} and R_{ei} represent series and parallel insulation losses, respectively. The self-inductance of the i^{th} unit is denoted by L_{Si}, and the mutual inductance between the i^{th} and j^{th} units is represented by $M_{i,j}$. The series capacitance is modeled by K_i, whereas the shunt capacitance to ground is represented by C_{ei}. Since the test winding does not include a magnetic core, a shielded copper cylinder is placed inside the winding to emulate the elements R_{ei} and C_{ei}, which correspond to the electric coupling between the winding and an equivalent core. All R-L-C-M components are calculated using a set of analytical expressions described in [11].

The FRA technique can be performed either in the time domain using a Low Voltage Impulse (LVI) or in the frequency domain using the Swept Frequency Response Analysis (SFRA) method [12, 13]. In the winding modelling, the SFRA approach is

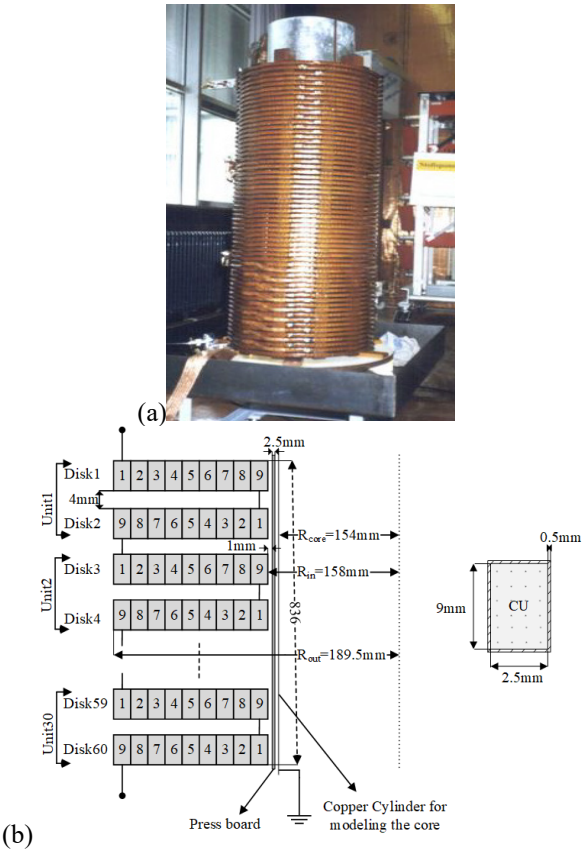

Figure 1. The configuration of the HV test winding (a), and its geometric dimensions (b)

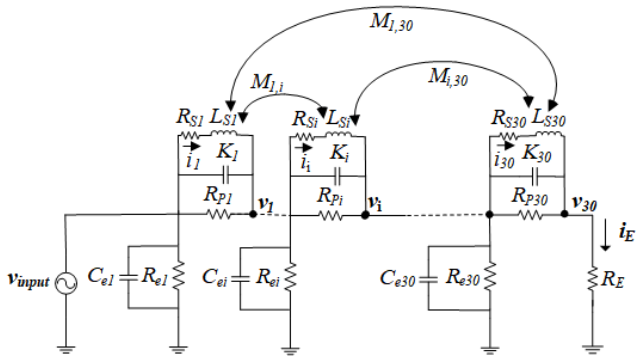

Figure 2. The detailed R-L-C-M model of the test winding comprises 30 units. R_E: grounding resistance.

employed to compute the FRs of the winding model shown in Fig. 2 under healthy conditions. In this method, a sinusoidal excitation voltage v_{input} with continuously varying frequency is applied to the model, and the resulting output v_{30} is calculated. The corresponding earth current i_E, flowing through a 50 Ω grounding resistor R_E, is then determined. Both v_{30} and i_E are obtained by applying Kirchhoff's laws to the detailed R-L-C-M network of Fig. 2, leading to the matrix formulation expressed in (1):

$$[Y][U] = [A][I] + [B_1]$$
$$[Z][I] = [A^T][U] + [B_2] \quad (1)$$

where:

$$I = [i_1 \quad \dots \quad i_{30}]^T,\ U = [v_1 \quad \dots \quad v_{30}]^T$$

Moreover, the elements A, B_1, B_2, and Z are provided in detail in [12], and Y is computed as:

$$[Y] = \begin{bmatrix} Y_{e1}+Y_{P1} & -Y_{P1} & 0 & \dots & \dots & 0 \\ -Y_{P1} & Y_{e2}+Y_{P1}+Y_{P2} & -Y_{P2} & 0 & \dots & 0 \\ \dots & \dots & \dots & \dots & \dots & \dots \\ 0 & \dots & \dots & -Y_{P28} & Y_{e29}+Y_{P29}+Y_{P30} & -Y_{P29} \\ 0 & \dots & \dots & \dots & -Y_{P29} & Y_{e30}+Y_{P30} \end{bmatrix}$$

where $Y_{Pi} = (j2\pi f K_{Pi} + 1/R_{Pi})$, $Y_{ei} = (j2\pi f C_{ei} + 1/R_{ei})$, and f denotes the applied frequency.

Using the applied voltage, v_{input}, and the calculated current, i_E, in the frequency domain, the required FR can be calculated as follows [13]:

$$FR(f) = \left| \frac{i_E(f)}{v_{input}(f)} \right| \tag{2}$$

2.1 Simulation of the Disc-to-Disc faults

To simulate a DDF at the i^{th} unit, a fault resistance, R_{SCi}, is inserted between its terminals as shown in Fig. 3. This resistance modifies the admittance matrix through the term, $Y_{SCi} = 1/R_{SCi,}$ which is added to the appropriate elements of the Y matrix as follows:

$$Y(i-1,i-1) = (Y_{P(i-1)} + Y_{Pi} + Y_{ei} + Y_{SCi})$$
$$Y(i-1,i) = Y(i,i-1) = -(Y_{Pi} + Y_{SCi})$$
$$Y(i,i) = (Y_{Pi} + Y_{P(i+1)} + Y_{e(i+1)} + Y_{SCi})$$

After applying v_{input} to the updated model (Fig. 3), the resulting i_E is computed and used to obtain the associated FR using Eq. (2). Applying a DDF with a specific R_{SCi} to each of the 30 units yields 30 distinct FRs. Furthermore, changing the value of R_{SCi} can alter the severity of DDF at the faulty unit. Therefore, applying n DDF with different severity levels to all units individually produces 30×n FRs, enabling systematic analysis of fault magnitude.

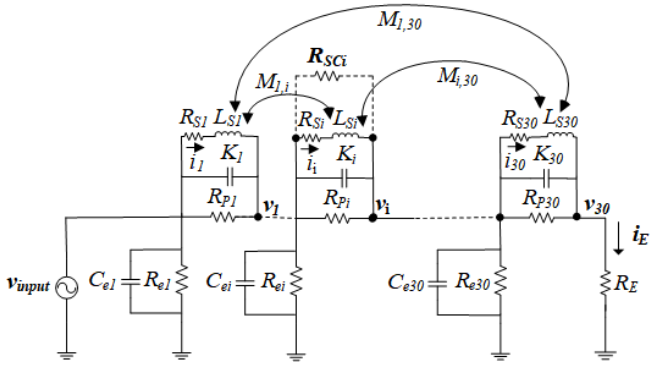

Figure 3. Applying the DDF to the detailed model in the i^{th} unit by linking its terminals to the fault resistance, R_{SCi}.

3 Validation of the modelling

To verify the obtained detailed model, its simulated FR under both healthy and SC conditions should be compared with the measured ones. Therefore, the LVI method is used to obtain the measured FRs of the winding. In this method, a low-voltage generator is used to apply an impulse voltage with front and tail times of 1.1 and 38.6 µs, respectively. Then, the output current is measured using a Rogowski Coil that records the current signal at 126 kHz to several MHz [12]. The input voltage and output current signals are then filtered and transformed to the frequency domain using the Fast Fourier Transform (FFT). Then, the measured FR can be calculated by dividing the current signal by the voltage signal. The FR of the winding is also measured after directly short-circuiting each consecutive pair of discs of the test winding. Therefore, in addition to the FR associated with the winding under healthy conditions, 30 measured FRs related to short-circuiting every two adjacent discs individually are also recorded.

To determine the accuracy of the winding model, the measured and simulated FRs obtained from the winding under healthy conditions are compared in Fig. 4. Furthermore, to further ensure the accuracy of the simulation, the measured and simulated FRs obtained after the occurrence of a DDF individually at units 12 and 15 with R_{SCi} = 0 Ω are compared in Fig. 5(a) and 5(b). It can be demonstrated from Fig. 4 and Fig. 5 that the acceptable agreement between the measured and simulated FRs proves the accuracy of the modelling. Therefore, the validated model can be used to simulate other DDFs with different severities.

Unit 15 is located in the middle of the model; therefore and after attention to the measured and simulated FRs obtained after applying DDF to all winding units individually, it can be observed a kind of symmetry between the FRs of the upper (units 1 to 15) and lower (units 16 to 30) halves of the winding. For clarity, from Fig. 6, the symmetry between the measured FRs resulting from direct short-circuiting the units 10 and 15 of the upper half by the fault resistance R_{SCi} = 0 Ω, with that related to units 16 and 21 of the lower half, respectively. Therefore, this symmetry can complicate discrimination between the DDF that occurred on a unit of the upper half and its corresponding one in the lower half.

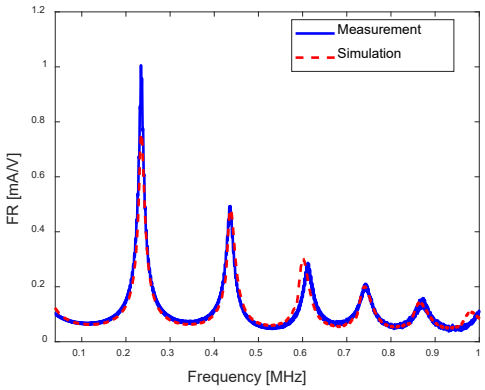

Figure 4. Comparison between simulated and measured FRs of the winding under intact condition.

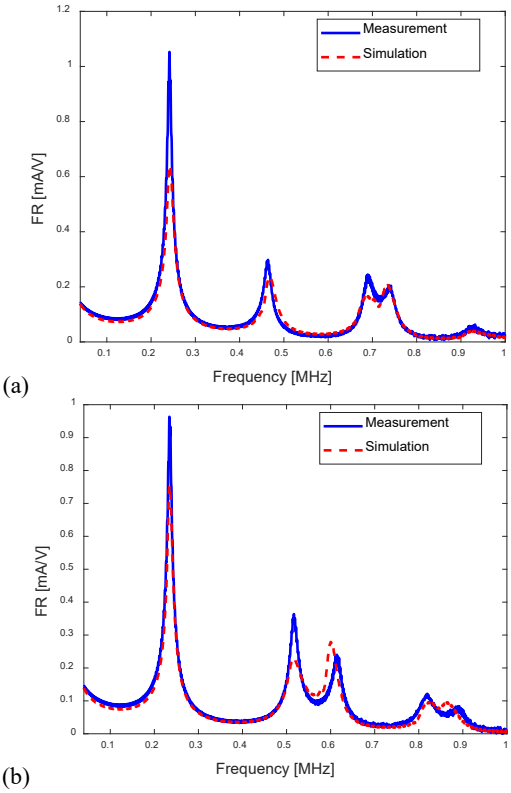

Figure 5. Comparison between simulated and measured FRs of the winding when occurrence SC with $R_{SCi} = 0\ \Omega$ at units 12 (a) and 15 (b).

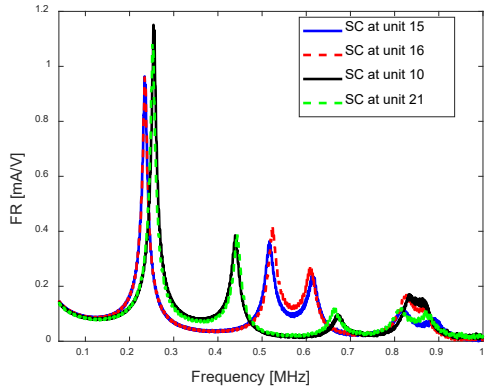

Figure 6. Symmetry in the measured frequency responses obtained from applying SC with $R_{SCi} = 0\ \Omega$ on units 15 and 16, and between units 10 and 21.

4 Kernel Principal Component Analysis (KPCA) method

Each FR of the winding related to healthy or DDF conditions is a nonlinear High-Dimensional (HD) data set containing D frequency samples; therefore, applying various DDFs with different severity levels to all winding units will produce N nonlinear FRs. Then, if these FRs are arranged in an HD matrix, called the Frequency Response Matrix (FRM), the dimensions of this matrix will be $N \times D$ as follows:

$$FRM = \begin{bmatrix} FR_1 \\ FR_2 \\ \dots \\ FR_{N-1} \\ FR_N \end{bmatrix} = \begin{bmatrix} FR_{1,1} & \dots & FR_{1,D} \\ FR_{2,1} & \dots & FR_{2,D} \\ \dots & \dots & \dots \\ FR_{N-1,1} & \dots & FR_{N-1,D} \\ FR_{N,1} & \dots & FR_{N,D} \end{bmatrix}_{N \times D}$$

To reduce the dimensionality of the FRM, an appropriate nonlinear dimension-reduction algorithm should be employed to extract key features and visualize them in a lower-dimensional space. Therefore, KPCA is a powerful nonlinear dimensionality reduction method that extends traditional PCA by first mapping the data to a high-dimensional space via a kernel function and then performing principal component analysis in that space [14]. Instead of explicitly computing the mapping function, this method uses the kernel trick to compute a Kernel Matrix (KM):

$$KM = \begin{bmatrix} KM_1 \\ KM_2 \\ \dots \\ KM_{N-1} \\ KM_N \end{bmatrix} = \begin{bmatrix} KM_{1,1} & \dots & KM_{1,N} \\ KM_{2,1} & \dots & KM_{2,N} \\ \dots & \dots & \dots \\ KM_{N-1,1} & \dots & KM_{N-1,N} \\ KM_{N,1} & \dots & KM_{N,N} \end{bmatrix}_{N \times N}$$

Each element of the KM is obtained using standard kernel functions, such as the Gaussian and polynomial kernels, which are described by expressions 3 and 4, respectively [14]:

$$KM_{i,j} = \exp\left(\frac{-\left\|FR_i - FR_j\right\|^2}{2\sigma^2}\right) \quad (3)$$

$$KM_{i,j} = (FR_i + FR_j + 1)^d \quad (4)$$

where $2\sigma^2$ is the width of the Gaussian kernel and d is a positive number determined by the trial-and-error method. In general, similar results should be obtained when selecting appropriate kernel parameters for expressions 3 and 4.

In the next step, the resulting KM must be centered, and the PCA algorithm must be used to extract the eigenvectors and eigenvalues of the calculated KM. By this method, each FR can be projected as a 2D feature point in a feature space through a weighted combination of kernel evaluations. This process not only reduces the dimensionality of the FRM but also preserves the geometric structure and nonlinear complexities of the FRs. For this reason, KPCA is highly effective and applicable to tasks such as error detection, pattern recognition, and classification [15].

By applying the PCA algorithm to the KM and calculating the related eigenvectors and eigenvalues, the high-dimensional FRM with dimensions of $N \times D$, including all FRs, will be transformed to a 2D matrix, including all related 2D Extracted Features (EFs) as follows:

$$EF == \begin{bmatrix} EF_{1,1} & EF_{1,2} \\ EF_{1,2} & EF_{2,2} \\ \dots & \dots \\ EF_{N-1,1} & EF_{N-1,2} \\ EF_{N,1} & EF_{N,2} \end{bmatrix}_{N\times 2}$$

More details on KPCA for calculating eigenvectors, eigenvalues, and 2D features are available in [14, 15].

5 Detecting Disc-to-Disc Faults

Validation of the winding model is a crucial prerequisite before introducing DDFs and analyzing their corresponding FRs. To this end, solid DDFs are first simulated by applying a fault resistance of R_{SCi} = 0 Ω sequentially to each unit of the model, and the resulting 30 FRs are computed and stored in a *FRM*. This procedure is then repeated for higher fault resistances of R_{SCi}=10, 30, 50, 70, and 100 Ω, which represent different fault severities, with the corresponding FRs appended to the *FRM*. As a result, in addition to the FR of the healthy winding, the *FRM* contains a total of 180 FRs corresponding to various DDF conditions. Moreover, a DDF with R_{SCi} = 37 Ω is applied to unit 13 as a new DDF to demonstrate the KPCA algorithm's ability to estimate the location and severity of any new fault along the winding. Then its FR is added to the *FRM*.

To show some simulated FRs of the model when exposing it to different DDFs, Figs. 7(a) and 7(b) present representative simulated FRs obtained when DDFs are applied to model units 1, 10, 15, 20, and 30 using fault resistances R_{SCi} = 0 and 50 Ω, respectively. As evident from these figures, increasing the fault resistance, corresponding to a reduction in fault severity, leads to a noticeable decrease in the magnitude of the FRs, while the resonance frequencies remain largely unchanged.

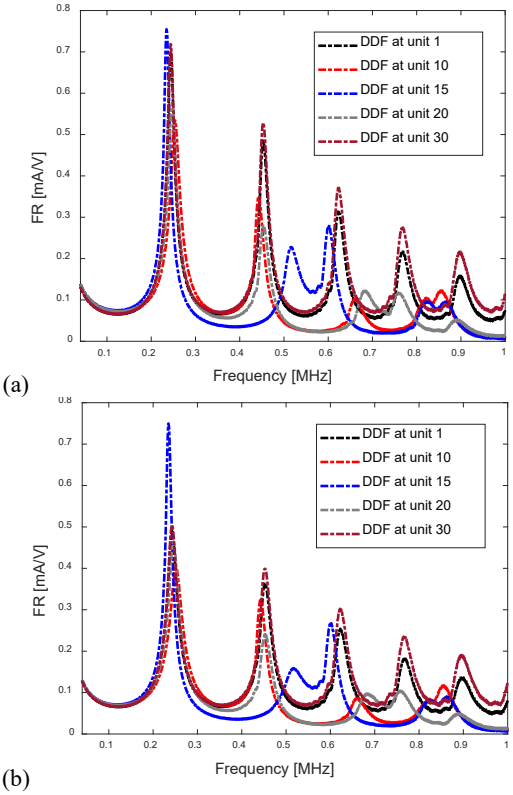

Figure 7. The simulated frequency responses of the winding when applying a DDF, with (a) R_{SCi} =0 Ω, and (b) R_{SCi} =50 Ω, to units 1, 10, 15, 20, and 30 individually

Applying the KPCA algorithm to the 182 FRs stored in the *FRM* will result in 182 *EFs* in the 2D space. Therefore, using the trial-and-error method, the KPCA with a polynomial kernel of degree 3 is applied to the *FRM*, and the resulting *EFs* are shown in Fig. 8(a). Furthermore, applying the Gaussian kernel with σ = 6 yields the *EFs* shown in Fig. 8(b). In these figures, the number of each unit is shown near its features. Moreover, it can be observed from Fig. 8(a) and 8(b) that the feature points associated with a unit are clustered. In addition, the symmetrical behaviour between the FRs related to the upper and lower units in the HD space is evident in the 2D space. For instance, the *EFs* for units 5 and 26 form two clusters with a very small distance. Furthermore, it is clear that increasing the fault resistance R_{SCi} shifts the related *EFs* towards the healthy conditions feature. Also, the *EF* obtained by applying the new DDF at unit 13 by R_{SCi} = 37 Ω is projected in the cluster associated with unit 13 and located between the *EFs* corresponding to DDFs with R_{SCi}= 30 and 50 Ω. Consequently, selecting the suitable parameters of the KPCA, including the degree of the polynomial and the variance of the Gaussian kernels, visualizes 2D feature points related to simulated FRs in separate clusters inside the feature space. Therefore, by comparing the distances between the feature points of the new DDFs that occur in the winding and the formed clusters in the 2D space, their locations and severities can be detected with acceptable accuracy.

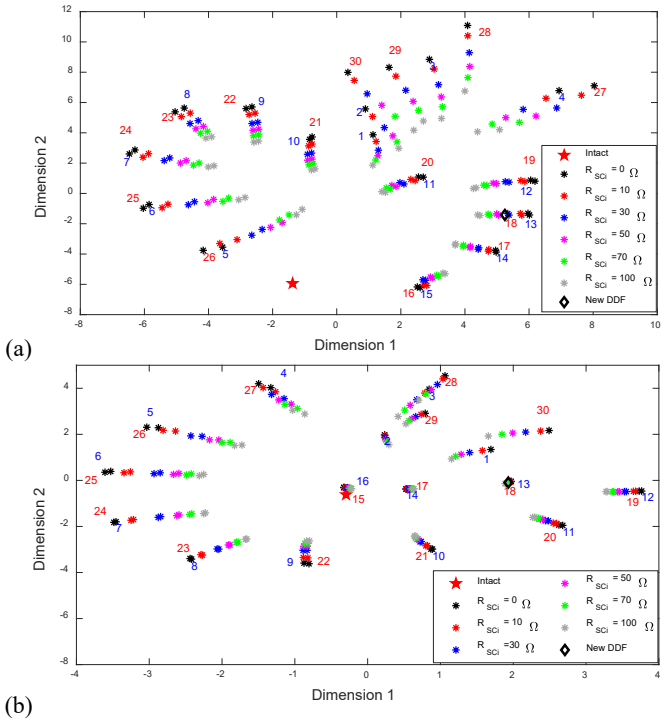

Figure 8. The extracted features obtained by applying the KPCA, with (a) polynomial, and (b) Gaussian kernels, to the FRs related to healthy and DDF conditions with R_{SCi} = 0, 10, 30, 50, 70, and 100 Ω, and FR associated with the new DDF.

6 Conclusion

This paper presented a comprehensive FRA-based framework for detecting and localizing disc-to-disc short-circuit faults in transformer windings using nonlinear feature extraction. A detailed R–L–C–M model of a specially fabricated HV disc winding was developed and validated through close agreement between simulated and experimentally measured frequency responses under both healthy and faulty conditions. The validated model enabled systematic simulation of disc-to-disc faults with varying locations and severities, providing a reliable dataset for advanced diagnostic analysis.

The KPCA algorithm was applied to the resulting high-dimensional FR data to extract salient nonlinear features and project them into a low-dimensional space. The results showed that KPCA effectively clusters FRs by fault location while preserving the progression of fault severity. Both polynomial and Gaussian kernels successfully revealed distinct feature groupings when appropriate kernel parameters were selected, confirming the suitability of KPCA for capturing the nonlinear behavior of FRA signatures associated with SC faults. Moreover, it was shown that the KPCA algorithm, by projecting the FRs of new DDFs into a 2D space, can reliably estimate their location and severity. These findings highlight the potential of combining detailed winding modeling, FRA measurements, and nonlinear dimensionality-reduction techniques as a powerful diagnostic tool for transformer winding condition assessment. Future work should focus on extending the presented methodology to more complex transformer configurations, including multi-winding and core-type transformers, and detecting other electrical and mechanical faults.

7 References

[1] Metwally, Ibrahim A. "Failures, monitoring and new trends of power transformers." *IEEE potentials* 30.3 (2011): 36-43.

[2] Li, Shuaibing, et al. "Interpretation of DGA for transformer fault diagnosis with complementary SaE-ELM and arctangent transform." *IEEE Transactions on Dielectrics and Electrical Insulation* 23.1 (2016): 586-595.

[3] Bigdeli, Mehdi, Mehdi Vakilian, and Ebrahim Rahimpour. "A probabilistic neural network classifier-based method for transformer winding fault identification through its transfer function measurement." *International Transactions on Electrical Energy Systems* 23.3 (2013): 392-404.

[4] Tarimoradi, Hadi, and Gevork B. Gharehpetian. "Novel calculation method of indices to improve classification of transformer winding fault type, location, and extent." *IEEE Transactions on Industrial Informatics* 13.4 (2017): 1531-1540.

[5] Abbasi, Ali Reza, and Mohammad Reza Mahmoudi. "Application of statistical control charts to discriminate transformer winding defects." *Electric Power Systems Research* 191 (2021): 106890.

[6] Ghanizadeh, Ahmad Javid, and G. B. Gharehpetian. "ANN and cross-correlation based features for discrimination between electrical and mechanical defects and their localization in transformer winding." *IEEE Transactions on Dielectrics and Electrical Insulation* 21.5 (2014): 2374-2382.

[7] Moradzadeh, Arash, and Kazem Pourhossein. "Early detection of turn-to-turn faults in power transformer winding: An experimental study." *2019 International Aegean Conference on Electrical Machines and Power Electronics (ACEMP) & 2019 International Conference on Optimization of Electrical and Electronic Equipment (OPTIM)*. IEEE, 2019.

[8] Moradzadeh, Arash, and Kazem Pourhossein. "Application of support vector machines to locate minor short circuits in transformer windings." *2019 54th International Universities Power Engineering Conference (UPEC)*. IEEE, 2019.

[9] Moradzadeh, Arash, et al. "Turn-to-turn short circuit fault localization in transformer winding via image processing and deep learning method." *IEEE Transactions on Industrial Informatics* 18.7 (2021): 4417-4426.

[10] Nosratian Ahour, Jafar, Saeed Seyedtabaii, and Gevork B. Gharehpetian. "Determination and localisation of turn-to-turn fault in transformer winding using frequency response analysis." *IET Science, Measurement & Technology* 12.3 (2018): 291-300.

[11] Aghmasheh, Reza, Vahid Rashtchi, and Ebrahim Rahimpour. "Gray box modeling of power transformer windings based on design geometry and particle swarm optimization algorithm." *IEEE transactions on power delivery* 33.5 (2018): 2384-2393.

[12] Rahimpour, Ebrahim, et al. "Transfer function method to diagnose axial displacement and radial deformation of transformer windings." *IEEE Transactions on power delivery* 18.2 (2003): 493-505.

[13] Rahimpour, Ebrahim, Mehdi Jabbari, and Stefan Tenbohlen. "Mathematical comparison methods to assess transfer functions of transformers to detect different types of mechanical faults." *IEEE transactions on power delivery* 25.4 (2010): 2544-2555.

[14] Dua, Wenxia, et al. "The Fault Detection of Power Transformers Based on Kernel Principal Component Analysis."

[15] Schölkopf, Bernhard, Alexander Smola, and Klaus-Robert Müller. "Kernel principal component analysis." *International conference on artificial neural networks*. Berlin, Heidelberg: Springer Berlin Heidelberg, 1997.

ТЕСЛИНИ ИНОВАЦИОНИ ДАНИ
TESLA INNOVATION DAYS
Belgrade, Serbia, April 7 - 8, 2025

DOI: 10.5937/TID250022G

METHODOLOGY FOR THE ASSESSMENT OF EXPOSURE OF WORKERS TO ELECTRIC AND MAGNETIC FIELDS DURING MAINTENANCE WORK ON DOUBLE-CIRCUIT TRANSMISSION OVERHEAD POWER LINES

Maja Grbić

Nikola Tesla Institute of Electrical Engineering, University of Belgrade, Republic of Serbia
maja@ieent.org

Abstract

Current practice for conducting works on maintenance of transmission double-circuit overhead power lines in the Republic of Serbia requires that, although the work is done on one line only, during work both lines have to be de-energized. This current practice in the Serbian transmission system is being changed in order to enable the possibility for de-energizing only the power line on which the work is done (passive system), so that the other power line on the same towers can stay in operation (active system). Before the approval for such a working practice is given, it is necessary to analyse all the potential risks to which the workers can be exposed and, if necessary, provide adequate protection measures. Such a practice includes a certain risk related to exposure of workers to electric and magnetic fields, which requires further analysis. While the work is being done on the passive system workers are exposed to electromagnetic field emitted by the active system. The paper presents a detailed analysis of the risk concerning the exposure of workers to electromagnetic field on the example of a typical double-circuit overhead power line. The analysis is based on results obtained by measurements of electric field strength and magnetic flux density. By measurements of electric field strength and magnetic flux density the field values corresponding to the time period of measurements are obtained. Since the power line voltages do not change significantly, results of electric field strength obtained by measurements can be directly used for the assessment of the exposure of workers. On the other hand, since the power line load currents are variable, the results of magnetic flux density obtained by measurements have to be analysed taking into account the active system load currents in the period of measurements, in order to come to the more general conclusion which has to take into consideration the most unfavourable working regime, leading to the highest exposure levels. When analysing the impact of electric and magnetic fields on workers it is assumed that the worker stays inside the working area defined by the procedure for conducting work on double-circuit power lines. The working area is defined as the space around passive system conductors up to the power line vertical axis. The work can be done from the tower directly or from the elevated platform, while the maximum distance between the tower and the working point is 30 m. Measurements of electric field strength and magnetic flux density are carried out at the measurement points located inside defined working area. In order to carry out measurements inside the working area the new measurement method was developed. The obtained results of electric field strength and magnetic flux density are compared to the action levels prescribed by current national regulations and Directive 2013/35/EU, based on which the conclusion on compliance of the obtained results with the aforementioned regulations is given.

Keywords: electromagnetic field, non-ionizing radiation, electric field strength, magnetic flux density, Directive 2013/35/EU, exposure of workers, double-circuit overhead power line.

1 Introduction

Overhead power lines are one of the most important sources of low frequency electromagnetic field in the environment, especially when their routes are located near residential areas [1, 2]. However, besides their influence on the environment and the general public, their impact on workers performing maintenance work on these power lines has to be analysed as well [3, 4] in order to ensure that the exposure of workers to electromagnetic field is within the prescribed limits.

Current practice for conducting works on maintenance of transmission double-circuit overhead power lines in the Republic of Serbia requires that during work both lines have to be de-energised, even in the case when the work is done on one line only. This practice is being changed in order to allow the possibility for de-energising only the power line on which the work is being done (passive system), so that the other power line on the same towers can stay in operation (active system). For that reason, it is necessary to analyse all the potential risks

to which the workers can be exposed and one of them is the exposure to electromagnetic field originating from the active system. This paper presents an analysis of the levels of electric and magnetic fields to which the workers are exposed during work on a typical 110 kV double-circuit overhead power line. The analysis is based on results obtained by measurements of electric field strength and magnetic flux density. The obtained results are compared to the action levels prescribed by relevant national and international regulations.

2 National and international legislation

The issue of exposure of workers to electromagnetic fields is addressed by Directive 2013/35/EU of the European Parliament and of the Council [5]. Directive [5] prescribes action levels which correspond to the measured or calculated values of electric and magnetic fields at the workplace. Action levels prescribed by Directive [5] for the power frequency (50 Hz) electric and magnetic fields are given in Table 1.

Table 1. Action levels for power frequency (50 Hz) electric field strength and magnetic flux density

Electric field strength		Magnetic flux density	
Low action level	High action level	Low action level	High action level
10 kV/m	20 kV/m	1000 μT	6000 μT

The action levels for power frequency (50 Hz) electric and magnetic fields in the Republic of Serbia are prescribed by the Rulebook on preventive measures to ensure safety and health of workers exposed to electromagnetic field [6] and they are equal to those prescribed by the Directive [5].

3 Assessment of exposure of workers to electric and magnetic fields

3.1 Measurement procedure

The testing was based on measurements of rms values of electric field strength and magnetic flux density.

The measurements were performed by using an electromagnetic field analyser and isotropic probes for electric field strength and magnetic flux density measurements. The probe for electric field strength measurements is cube-shaped, with a 10 cm edge. The probe for magnetic flux density measurements is sphere-shaped, with a cross-sectional area of 100 cm^2. Both probes ensure simultaneous measurements of all three spatial components of field vectors, based on which the instrument shows the resultant values of the field vectors. The measuring system fulfils the requirements of the standard [7].

Procedures for measurements of electric field strength and magnetic flux density in the vicinity of overhead power lines are given in [7-11]. However, these procedures mainly refer to the assessment of exposure of the general public living in the vicinity of overhead power lines and therefore they are not entirely suitable for the assessment of exposure of workers performing maintenance works on overhead power lines. For that reason, a new measurement procedure was developed and applied in order to ensure measurements of unperturbed field in the working area.

When analysing the impact of electric and magnetic fields on the workers, it was assumed that the worker stays inside the area defined by the procedure for conducting work on double-circuit power lines [12]. The working area is defined as the space around the passive system conductors up to the power line vertical axis. The work can be done from the tower directly or from the elevating work platform. Potential working areas near the tower is presented in Figure 1. In this figure, the mark l indicates the approach distance from the active system conductors, while the marks I, II and III indicate work zones near the overhead power line prescribed by [12].

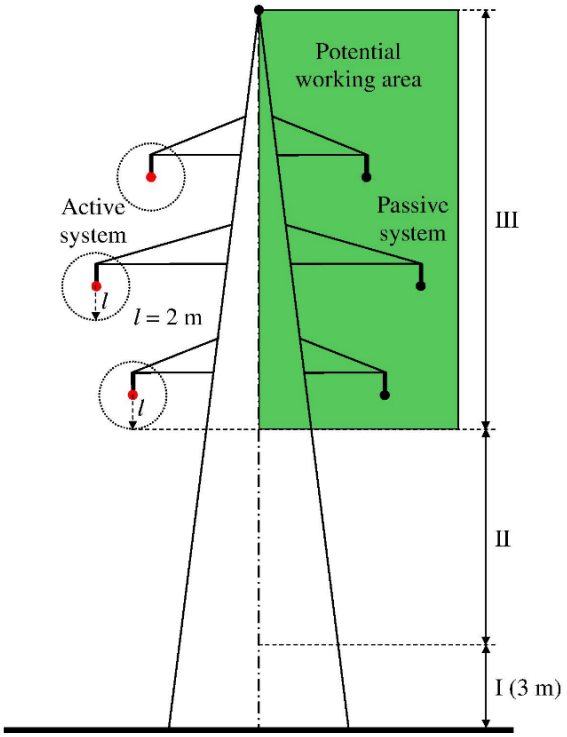

Figure 1. Working area at 110 kV double-circuit overhead power line referring to the work performed at the tower

Measurements of electric field strength and magnetic flux density were carried out at the measurement points located inside the defined working area in the close vicinity of the tower. These measurements were performed along the vertical profiles which were in line with the power line phase conductors and ground wire. During the measurements, the measuring instruments were attached to the aforementioned conductors by insulating ropes which were positioned from an elevating work platform. The procedure of attaching the insulating ropes to the phase conductors and ground wire is shown in Figure 2. The probes for electric and magnetic fields attached to the conductors are shown in Figures 3 and 4.

The measurements were performed at numerous measurement points along the vertical profiles. The first measurement point was located at the height of 1 m above the ground. After that the measurement height was increased by 1 m step.

a)

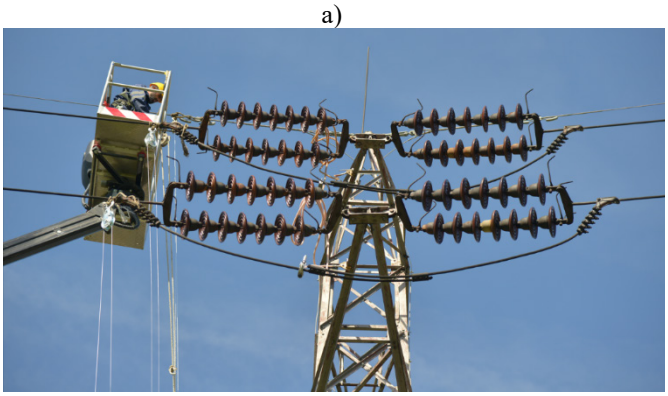

b)

Figure 2. The procedure of attaching the insulating ropes to the phase conductors and ground wire

Figure 3. The probes for electric and magnetic fields attached to the phase conductors

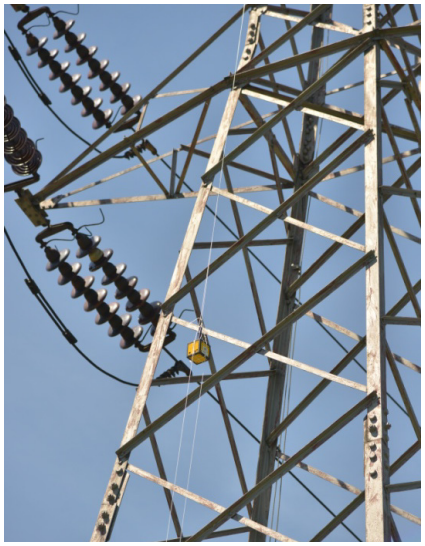

a)

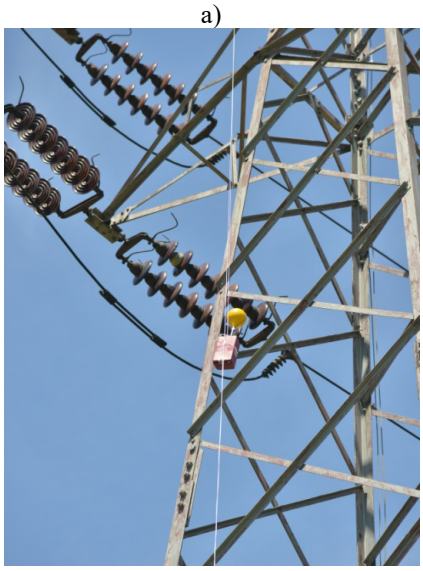

b)

Figure 4. The probes for electric (a) and magnetic (b) fields attached to the conductors

During electric field strength and magnetic flux density measurements, the option of automatic measurement regime with predefined time step was used. Several electric field strength and magnetic flux density measurements were carried out at each measurement point, while the average value of these results represents the final measurement result at that measurement point. During the entire period of electric field strength and magnetic flux density measurements the data on values of voltages and currents in all three phases of the active system were provided. The data on power line load currents are significant for the assessment of maximum magnetic flux density values which would correspond to the maximum power line load.

3.2 Measurement results

During the testing, the one line was in normal operating regime (active system), while the other line was de-energised (passive system). In this situation, workers doing maintenance work on the passive system are exposed to electric and magnetic fields

originating from the active system. For that reason, the information on levels of electric and magnetic fields in the potential working area presented in Figure 1 should be obtained. The highest values of electric and magnetic fields were obtained at the vertical profile which is aligned with the power line axis since this profile is the closest one to the active system. Power line geometry, i.e. conductor heights and distances from the power line axis next to the tower are presented in Figure 5. In Figure 5, the mark P_{gw} refers to the vertical measurement profile aligned with the power line axis, i.e. with the ground wire. Vertical profile P_{p4} is aligned with the phase 4, while the profile P_{p8} is aligned with the phase 8.

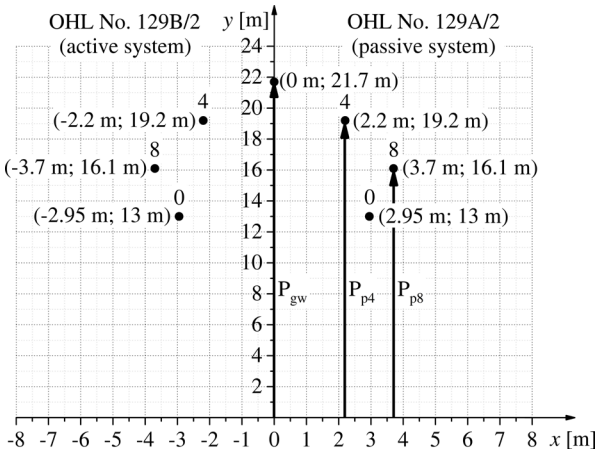

Figure 5. Geometry of the power line next to the tower during electric and magnetic field measurements

The results of electric field strength measurements are presented in Figure 6. The average values of the active line voltages during the period of electric field strength measurements are also given in Figure 6. Marks in this figure indicate the following:

E_m – the measured value of electric field strength (represents the average value of several measurement results at the specified measurement point),

h – the height of the measurement point above ground,

U_{04}, U_{48}, U_{80} – the average values of active line voltages in the period when the measurements of electric field strength were conducted.

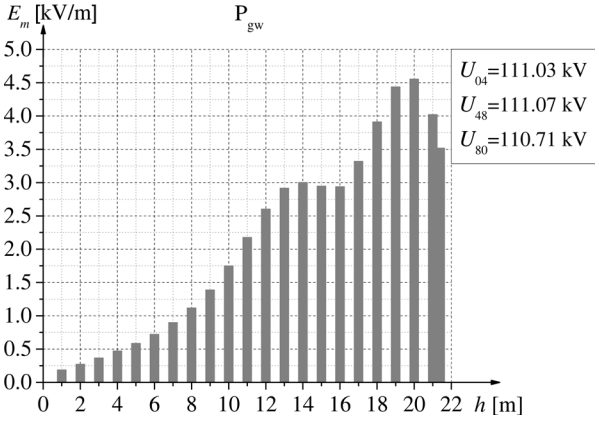

Figure 6. Results of electric field strength measurements next to the tower along the vertical profile P_{gw}

The highest measured value of electric field strength was 4.56 kV/m. On the basis of the presented results, it can be concluded that the values of electric field strength in the potential working area are below the low action level of 10 kV/m.

The results of magnetic flux density measurements are presented in Figure 7. The average values of the active line currents during the period of magnetic flux density measurements are also given in Figure 7. Marks in this figure indicate the following:

B_m – the measured value of magnetic flux density (represents the average value of several measurement results at the specified measurement point),

h – the height of the measurement point above ground,

I_0, I_4, I_8 – the average values of active line currents in the period when the measurements of magnetic flux density were conducted.

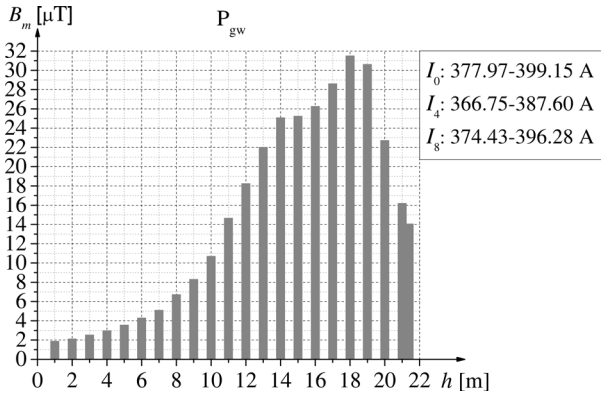

Figure 7. Results of magnetic flux density measurements next to the tower along the vertical profile P_{gw}

The highest measured value of magnetic flux density was 31.51 μT. At the moment of this measurement, the active line load currents in phases 0, 4 and 8 were 385.15 A, 374.41 A and 383.60 A, respectively. The maximum load current of the analysed power line is 880 A. Based on the extrapolation of the highest measured value of magnetic flux density it can be concluded that the value of magnetic flux density in the case of maximum power line load current will not exceed the level of 75 μT. Based on the obtained results, it can be concluded that even in the situation when the active line current is equal to its maximum load current the values of magnetic flux density in the potential working area are significantly below the low action level of 1000 μT.

4 Conclusion

The paper presents the detailed analysis of the risk related to the exposure of workers to electric and magnetic fields during work on a 110 kV double-circuit overhead power line. The situation when the work is being done on de-energised system while the other system on the same towers is in operation was analysed. The analysis was based on measurements of electric field strength and magnetic flux density. In order to ensure measurements of unperturbed field in the working area, the new measurement procedure was developed and applied. The highest value of electric field strength obtained by

measurements was 4.56 kV/m, while the highest measured value of magnetic flux density was 31.51 μT. The highest value of magnetic flux density obtained by extrapolation of the measured value was 75 μT and it refers to case when the power line load current is equal to its maximum current. Based on the presented results, it is concluded that the obtained values of electric field strength and magnetic flux density are below the low action levels of 10 kV/m and 1000 μT, prescribed by national regulations and the Directive 2013/35/EU. Therefore, in the analysed case the maintenance work can be carried out without additional equipment for protection from electromagnetic field.

5 Acknowledgements

This work was supported in part by the Ministry of Science, Technological Development and Innovation of the Republic of Serbia under the Contract on the realization and financing of the scientific research work of research and innovation organizations in 2025.

6 References

[1] M. Grbić, J. Mikulović, D. Salamon, "Influence of Measurement Uncertainty of Overhead Power Line Conductor Heights on Electric and Magnetic Field Calculation Results", Int. J. Electr. Power Energy Syst., vol. 98, (2018), 2017, pp. 167–175.

[2] M. Grbić, D. Salamon, J. Mikulović, "Analysis of Influence of Measuring Voltage Transformer Ratio Error on Single-Circuit Overhead Power Line Electric Field Calculation Results", Electr. Power Syst. Res., vol. 166, 2018, pp. 232–240.

[3] M. Grbić, A. Pavlović: "Exposure of Workers to Electric and Magnetic Fields during Maintenance Work on Double-Circuit Overhead Power Lines", The 48th CIGRE Session (e-session), International Council on Large Electric Systems – CIGRE, August 24 - September 3, 2020, Proceedings, Paper No. B2-304.

[4] M. Grbić, A. Pavlović: "Analysis of the Exposure of Workers to Electric and Magnetic Fields during Maintenance Works on Distribution Overhead Power Lines", The 27th International Conference and Exhibition on Electricity Distribution – CIRED, Rome, Italy, June 12–15, 2023, Paper No. 11234, DOI: 10.1049/icp.2023.0846.

[5] Directive 2013/35/EU of the European Parliament and of the Council of 26 June 2013 on the minimum health and safety requirements regarding the exposure of workers to the risks arising from physical agents (electromagnetic fields) (20th individual Directive within the meaning of Article 16(1) of Directive 89/391/EEC) and repealing Directive 2004/40/EC, Official Journal of the European Union, June 29, 2013.

[6] Rulebook on preventive measures to ensure safety and health of workers exposed to electromagnetic field, Official Gazette of the Republic of Serbia No. 111/2015, published on December 29, 2015.

[7] IEC 61786, "Measurement of DC magnetic, AC magnetic and AC electric fields from 1 Hz to 100 kHz with regard to exposure of human beings – Part 1: Requirements for measuring instruments", 2013.

[8] IEC 61786, "Measurement of DC magnetic, AC magnetic and AC electric fields from 1 Hz to 100 kHz with regard to exposure of human beings – Part 2: Basic standard for measurements", 2014.

[9] EN 62110, "Electric and magnetic field levels generated by AC power systems – Measurement procedures with regard to public exposure", 2009.

[10] EN 50413, "Basic standard on measurement and calculation procedures for human exposure to electric, magnetic and electromagnetic fields (0 Hz – 300 GHz)", 2019.

[11] Technical guide for measurement of low frequency electric and magnetic fields near overhead power lines, CIGRE Working Group C4.203, 2009.

[12] Instructions for working in the vicinity of high voltage on double-circuit overhead power lines, Public Enterprise Elektromreža Srbije, Technical Guidelines TU-DV-10, edition No. 1, December 2015. (In Serbian).

ТЕСЛИНИ ИНОВАЦИОНИ ДАНИ
TESLA INNOVATION DAYS
Belgrade, Serbia, April 7 - 8, 2025

DOI: 10.5937/TID25027D

INNOVATION IN EMI SHIELDING MATERIALS INTEGRATED IN GRINSHIELD PROJECT – TWINNING FOR NEW GRAPHENE BASED NANOMATERIALS

Slađana Dorontić**, Svetlana Jovanović

Vinča Institute of Nuclear Sciences-National Institute of the Republic of Serbia, University of Belgrade, P.O. Box 522, 11000 Belgrade, Serbia

**sladjana.dorontic@vin.bg.ac.rs*

Abstract

In the last decade, scientific interest in and industrial needs for new electromagnetic (EM) shielding materials have significantly increased due to technological developments in the telecommunication and electronic sectors. The world market for shielding materials demands new, lightweight, flexible, and durable shielding materials. At the same time, ecological aspects in the production process must be considered. Priority will be given to materials produced in an eco friendly and sustainable manner. Due to its light weight, flexibility, chemical stability, and electrical properties, graphene and its derivates are promising candidates for future EM shielding materials. The GrInShield project is focused on developing graphene-based composites able to block the propagation of electromagnetic waves from low (150 kHz) to high frequencies (8-12 GHz). The purpose of these materials will be the protection of electronic devices and sensitive instruments from secondary EM waves and wearable protection by developing textiles for professional clothes. Our research showed that graphene oxides in the form of free-standing films show very low EM shielding efficiency (~ 2 dB) while after chemical reduction, materials with the same thicknesses (13 ±0.32 μm) become more efficient (~ 6 dB). EM shielding efficiency was increased by including metal-based nanomaterials in graphene composites. Namely, adding 50 wt% silver nanowires (AgNWs) to graphene oxide free-standing films improved EM shielding efficiency to -12.1 dB, while 80 wt% of AgNWs led to -33.3 dB. When these materials were chemically reduced, the EM shielding effectiveness was 24.17 dB and -35.6 dB. Recently, as an answer to the high price of graphene and low production, new methods are developing for graphene-based nanomaterials production, where precursors are different biomasses. Precursor carbonization occurs during the process of heating in an oxygen-free atmosphere. These materials are known as biochar, and they were studied mainly as sorbents. GrInShield team produced biochars using fruit-processing biowastes. After mixing with the polymer sodium silicate resin, a flexible, 0.2 cm thin composite showed EM shielding effectiveness, blocking above 70% of the incident waves. These results indicated the outstanding potential of biochars and graphene-metallic nanomaterials composites for their application in EM shielding.

Keywords: graphene, graphene oxide, shielding, composites.

1 Introduction

The growing need for information flow in modern society has caused rapid progress in the development of electrical devices [1]. Communication technology, wearable and portable devices, are increasingly used. This technological leap has led to the presence of electromagnetic (EM) waves from artificial sources in everyday life [2]. Before World War II, no importance was attached to the health effects of EM radiation, as it was considered non-ionizing and believed to be unable to alter the structure of biomolecules [3]. When the first harmful implications, such as hormonal imbalances [4], circadian rhythm disorders [5], cellular cation levels, and memory alterations [6], were noticed, the concept of EM pollution was born. Later, it was found that the EM radiation at certain frequencies (radio frequencies – RF, used in mobile communications and radar) can interact with the functions of electrosensitive systems, such as the cardiovascular and nervous system, through thermal and non-thermal effects, hormonal signalling pathway, etc [3]. Additionally, EM waves ranging from extremely low (EL) to RF-EM waves influence animal population dynamics [7], life cycle [8], orientation [9], and migrations [10], as well as plant metabolism [11]. Besides effects on human health and the environment, EM interference (EMI) is another problem [3]. However, electrical devices may interact with vulnerable medical equipment such as pacemakers, infusion pumps, etc., and reduce their lifespan. Thus, new solutions for EMI shielding are needed.

Suitable materials for EMI shielding should be thin, elastic, chemically inert, flexible, moisture resistant, and ideally be produced through an environmentally friendly process [12]. Metal-based nanocomposites, foams, and fabrics

are commonly used for EMI shielding because of their excellent electrical conductivity, but they are also corrosive, less flexible, and costly to maintain [13]. In search of better options, lightweight and cost-effective materials such as conductive polymer composites (CPCs), silicone rubbers, and MXenes are being developed.

Among potential EMI shielding materials, graphene and its composites have been the focus of research for the last few years. This is a 2D nanomaterial, built of sp^2 hybridized C atoms organized in a hexagonal crystal lattice [12]. Each C atom is covalently bonded to three neighbours, where one electron per C atom leaves unpaired. Orbitals of free electrons overlap, forming a π-cloud where electrons can move easily. Due to such a structure, graphene is distinguished by its unique electrical, mechanical, and chemical properties [12]. Their electrical conductivity of up to 10^5 S/m [14], large surface area, lightweight nature, and mechanical strength make graphene a promising material for blocking EM waves.

Next to graphene, recent researches are directed toward highly environmentally friendly, easy-to-produce materials - biochars obtained from biomass and biowaste resources [2]. After the carbonization of natural resources at high temperatures up to 900°C in an oxygen-restricted atmosphere, an extra-hard, thermal, and electrically stable material can be obtained [15]. Solely, or in combination with polymers, biochars represent sustainable, renewable, eco-friendly, and affordable materials that can serve as filters for EM waves [2].

In this review, we summarized the latest publications related to applications of graphene and its composites, as well as biochar for EMI shielding purposes.

1.1. Graphene oxide and its composites in EMI shielding

In comparison with pristine graphene, graphene oxide (GO) and reduced graphene oxide (rGO) have several advantages, including cost-effectiveness and feasibility. GO is the oxidized form of graphene, with a high ratio of oxygen-containing moieties bonded to the graphene layer. It makes GO dispersible in water [16]. Furthermore, oxidation tunes the GO band gap and increases defects in the graphene sheets. The structure can be particularly recovered through graphene reduction. Reduced GO (rGO) possesses higher electrical conductivity than GO [12]. Due to their large surface area, both GO and rGO are suitable for covalent and non-covalent bonding, which allows them to be combined with polymers, nanoparticles, etc., in hybrid composites.

Within a study, Stefanovic et al. produced GO using modified Hummer's method and the electrochemical oxidation and exfoliation of high-order pyrolytic graphene (HOPG) [17]. They treated both samples at 500°C and 800°C for 1 h under a pure NH_3 gas. The N-doped, reduced GO with the highest N ratio (11.25 ± 0.08 at%) and high electrical conductivity was obtained. By measuring shielding effectiveness (SE), it is found that this sample can block EM waves in the frequency range of 8-12 GHz (Figure 1.), mainly through absorption.

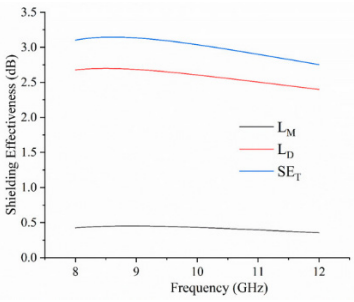

Figure 1. SE_T, L_M, and L_D values for GO-500, measured in the 8–12 GHz frequency range. Figure reprinted from reference. [17] Copyright 2025, MDPI AG. Licence is under Creative Commons.

Later, Prekodravac Filipović et al. modified GO and rGO free-standing films via gamma irradiation at low (50 kGy) and high doses (300 kGy) in the two types of media: air and isopropyl alcohol [18]. Raman, Infrared spectroscopy, scanning electron microscopies, and contact angle measurements indicate structural alterations, changes in defect density, and roughness. Gamma-irradiated rGO showed extraordinary SE of 20 dB in the X band.

New EMI shielding material based on GO and silver nanowires (AgNWs) composite in different mass ratios of each component was structured by Milenković et al. [19]. UV-Vis, Infrared, and Raman spectroscopies, as well as thermogravimetric analysis, confirmed that the interaction between GO and AgNWs was established. For the first time, the type of interaction between these two materials in the composite was investigated by density functional theory (DFT) analysis. The interaction energy between GO and AgNWs was calculated to be −81.9 kcal/mol. DFT results showed interfacial polarization at the heterointerface via charge transfer and accumulation at the interface, enhancing the efficiency of EMI shielding. SE values for composites with different mass ratios of 5:5, 3:7, and 1:9 of GO and AgNWs within the X band ranged from 0.9 and 4.5 dB.

A composite sandwich structure based on silver nanowires placed between GO or rGO layers was fabricated by Kepić et al. [20]. The obtained composite was tested as an EMI shielding platform within a broad microwave range.

Furthermore, Kepić et al. combined GO with platinum nanoparticles (PtNPs) created on the GO surface during exprosre to a low dose of gamma rays (10 and 20 kGy) [16]. Irradiation led to a reduction of hexachloroplatinic acid into PtNPs and partial reduction of GO. DFT analysis revealed a significant difference in the electrical conductivity of GO and PtNPs. That can contribute to charge reorganization along the contact area. These conductive clusters represent an excellent platform for EMI shielding. The shielding efficiency conducted in the X band showed that the composites blocked 77% of the incident EM waves at the central frequency of 10 GHz (Figure 2.).

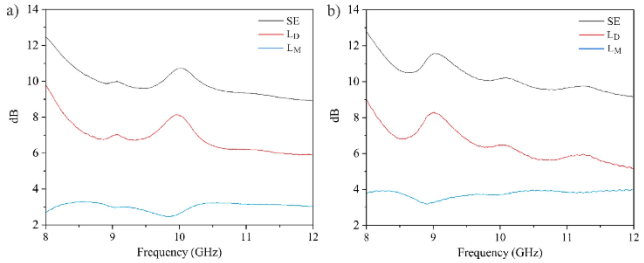

Figure 2. L_D, L_M, and SE values for (a) GO-PtNPs prepared at 1 kGy and (b) GO-PtNPs prepared at 20 kGy. Figure reprinted from the source [16]. Copyright © 2025, under a CC BY license.

GO/AgNWs composite can be integrated into various conductive polymers to improve shielding efficiency. Gajić et al. have developed a composite based on polypyrrole (PPy), GO, and AgNWs through oxidative polymerisation of pyrrole monomer incorporated in polycaprolactone (PCL) monomer [21]. SEM analysis showed granular PPy, layered GO, and fibrous AgNWs. Results of thermomechanical analysis confirmed that GO contributed to the glass transition, while AgNWs improved toughness and energy dissipation. During the examination of SE in the X band, it was revealed that pure PPy showed poor shielding viability, while the composite with GO and AgNWs showed significant performance (average SE of 16.05 dB).

The same research group investigated the comparative impact of rGO, AgNWs, and their hybrid rGO-AgNWs on the EMi shielding capability of polyaniline (PANI) based flexible films prepared using a PCL matrix [22]. A nanocomposite was fabricated by oxidative polymerization of aniline in the presence of rGO or AgNWs, separately or in their hybrid. Then, the composite was dispersed in the PCL matrix and cast into corresponding films. Morphological and structural analysis conducted by SEM, Raman, and FTIR spectroscopies revealed a 3D conductive network consisting of PANI that is coated on both rGO layers as well as AgNWs. Thermal and thermomechanical analysis showed excellent thermal stability of all composite systems. The highest EMI shielding SE of ~7.2 dB was observed for the PANI/rGO/PCL film, whereas AgNWs were found to partially disrupt the conductive network, resulting in a decrease in SE to ~5.6 dB.

1.2. Biomass and biowaste-derived EMI shielding solutions

Recently, considerable attention has been paid to carbonized biomass and biowaste materials in terms of EMI shielding applications. Milenković et al. showed an innovative approach for the production of biochar from stillage – agricultural biowaste remaining from apple and quince schnapps distillation [23]. The initial biowaste was mixed with potassium hydroxide, which served as an activator, and carbonized at 850°C in a nitrogen atmosphere. According to (Brunauer–Emmett–Teller analysis, high specific surface area values, 1618 m^2/g and 1260 m^2/g for biochars from quinces and apples' stillage, respectively, were noticed. Also, gas sorption analysis revealed mesoporous structures of the samples. Biochars structure analysis using Raman, X-ray diffraction (XRD), and X-ray photoelectron spectroscopies proved the presence of the graphitic domains in biochars. EMI shielding measurements in X band showed SE values of 10.7 dB and 13.5 dB for apple and quince-derived biochar, respectively, which correspond to the blocking of 69.4% and 78.5% of incident EM waves.

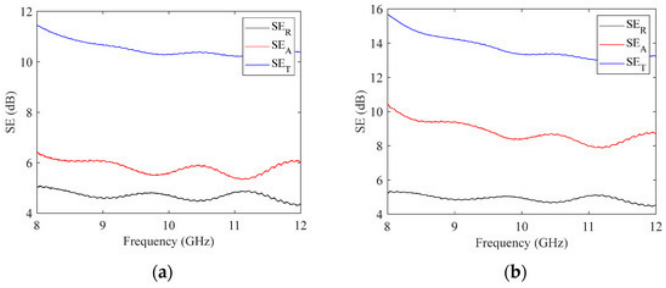

Figure 3. EMI performance of BA (a) and BQ (b): SE_R, SE_A, and SE_T, in the frequency range 8–12 GHz. Figurereprinted from reference [23]. Copyright 2024, MDPI AG. Licence is under Creative Commons.

EMI SE values obtained by exploring the shielding capacity of graphene, its composites, and biochar within the X band are summarized in Table 1.

Table 1. EMI SE values of rGO, composites based on GO and biochars.

Material	EMI SE (dB) or % of blocked incident waves	Ref.
γ-irradiated rGO	20 dB	[18]
GO/AgNWs nanocomposite	0.9 – 4.5 dB	[19]
GO/PtNPs nanocomposite	blocked 77% of the incident EM waves	[16]
GO/AgNWs/PPy hybrid	16.05 dB	[21]
rGO/AgNWs/PANI hybrid	~5.6 dB	[22]
Apple-derived biochar Quince-derived biochar	10.7 dB 13.5 dB	[23]

2. Conclusion

The increasing exposure to electromagnetic waves in modern technologies created the need for new, efficient, and lightweight EMI shielding materials. Graphene-based composites have proven to be a promising solution, as they combine high electrical conductivity with low weight and good mechanical flexibility. Desirable results can be achieved by integrating graphene with metal nanoparticles, conductive polymers, and using sustainable materials such as biochar. Although significant progress has been made, further research is still required to adapt these materials for practical applications and large-scale production.

3. Acknowledgements

This research was supported by the European Union's Horizon Europe Coordination and Support Actions programme under grant agreement No 101079151—GrInShield. Authors thank the Ministry of Science, Technological Development and Innovation of the Republic of Serbia (grant number 451-03-136/2025-03/ 200017).

4. References

[1] J. Wei *et al.*, 'Sandwich structured cellulose-based composite for electromagnetic interference shielding, infrared stealth and Joule heating', *Carbohydrate Polymers,* vol. 367, p. 123979, 2025/11/01/ 2025.

[2] D. Marinković *et al.*, 'New Electromagnetic Interference Shielding Materials: Biochars, Scaffolds, Rare Earth, and Ferrite-Based Materials', *Nanomaterials*, vol. 15, no. 7. doi: 10.3390/nano15070541.

[3] J. Prekodravac Filipovic *et al.*, 'Electromagnetic Interference in the Modern Era: Concerns, Trends, and Nanomaterial-Based Solutions', *Nanomaterials*, vol. 15, no. 20, p. 1558. doi: 10.3390/nano15201558.

[4] B. Selmaoui and Y. Touitou, 'Association Between Mobile Phone Radiation Exposure and the Secretion of Melatonin and Cortisol, Two Markers of the Circadian System: A Review," (in eng), *Bioelectromagnetics,* vol. 42, no. 1, pp. 5-17, Jan 2021.

[5] Y. Touitou, B. Selmaoui, and J. Lambrozo, 'Assessment of cortisol secretory pattern in workers chronically exposed to ELF-EMF generated by high voltage transmission lines and substations,' *Environment International,* vol. 161, p. 107103, 2022/03/01/ 2022.

[6] I. Hasan, M. Rubayet Jahan, M. Nabiul Islam, and M. Rafiqul Islam, 'Effect of 2400 MHz mobile phone radiation exposure on the behavior and hippocampus morphology in Swiss mouse model', *Saudi Journal of Biological Sciences,* vol. 29, no. 1, pp. 102-110, 2022/01/01/ 2022.

[7] O. Marushchak, O. Nekrasova, O. Oskyrko, V. Voitenko, and D. Zhytnyk, 'Electromagnetic field influence on peculiarities of rana temporaria linnaeus, 1758 (ANURA, RANIDAE) ONTOGENY', *Environmental Research, Engineering and Management,* vol. 75, pp. 82-89, 09/03 2019.

[8] D. P. Fey, M. Jakubowska, M. Greszkiewicz, E. Andrulewicz, Z. Otremba, and B. Urban-Malinga, 'Are magnetic and electromagnetic fields of anthropogenic origin potential threats to early life stages of fish?', (in eng), *Aquat Toxicol,* vol. 209, pp. 150-158, Apr 2019.

[9] B. Leberecht *et al.*, 'Broadband 75–85 MHz radiofrequency fields disrupt magnetic compass orientation in night-migratory songbirds consistent with a flavin-based radical pair magnetoreceptor', *Journal of Comparative Physiology A,* vol. 208, no. 1, pp. 97-106, 2022/01/01 2022.

[10] B. Leberecht *et al.*, 'Upper bound for broadband radiofrequency field disruption of magnetic compass orientation in night-migratory songbirds', *Proceedings of the National Academy of Sciences,* vol. 120, no. 28, p. e2301153120, 2023/07/11 2023.

[11] S. Kaur, A. Vian, S. Chandel, H. P. Singh, D. R. Batish, and R. K. Kohli, 'Sensitivity of plants to high frequency electromagnetic radiation: cellular mechanisms and morphological changes', *Reviews in Environmental Science and Bio/Technology,* vol. 20, no. 1, pp. 55-74, 2021/03/01 2021.

[12] S. Jovanović, M. Huskić, D. Kepić, M. Yasir, and K. Haddadi, 'A review on graphene and graphene composites for application in electromagnetic shielding', *Graphene and 2D Materials,* vol. 8, no. 3, pp. 59-80, 2023/12/01 2023.

[13] S. Zecchi *et al.*, 'A Comprehensive Review of Electromagnetic Interference Shielding Composite Materials', *Micromachines*, vol. 15, no. 2. doi: 10.3390/mi15020187.

[14] C. Fang, J. Zhang, X. Chen, and G. J. Weng, 'Calculating the Electrical Conductivity of Graphene Nanoplatelet Polymer Composites by a Monte Carlo Method', *Nanomaterials*, vol. 10, no. 6. doi: 10.3390/nano10061129.

[15] E.-S. Khater, A. Bahnasawy, R. Hamouda, A. Sabahy, W. Abbas, and O. M. Morsy, 'Biochar production under different pyrolysis temperatures with different types of agricultural wastes', *Scientific Reports,* vol. 14, no. 1, p. 2625, 2024/02/01 2024.

[16] D. Kepić *et al.*, 'Investigation of the interactions and electromagnetic shielding properties of graphene oxide/platinum nanoparticle composites prepared under low-dose gamma irradiation', *Scientific Reports,* vol. 15, no. 1, p. 26924, 2025/07/24 2025.

[17] A. Stefanović *et al.*, 'A New Route to Tune the Electrical Properties of Graphene Oxide: A Simultaneous, One-Step N-Doping and Reduction as a Tool for Its Structural Transformation', *Molecules*, vol. 30, no. 17, p. 3579. doi: 10.3390/molecules30173579.

[18] J. P. Filipovic *et al.*, 'Sustainable gamma irradiation strategy for GO and rGO modification: Impact on electromagnetic interference shielding efficiency', *Chemical Engineering Journal Advances,* vol. 24, p. 100873, 2025/11/01/ 2025.

[19] M. Milenković *et al.*, 'Study of Graphene Oxide and Silver Nanowires Interactions and Its Association with Electromagnetic Shielding Effectiveness', *International Journal of Molecular Sciences*, vol. 25, no. 24, p. 13401. doi: 10.3390/ijms252413401.

[20] D. Kepić, A. Pantić, W. Saeed, M. Yasir, and S. Jovanović, 'Microwave electromagnetic shielding of free-standing composites of silver nanowires sandwiched between graphene oxide or reduced graphene oxide layers', *Journal of Micro and Bio Robotics,* vol. 21, no. 1, p. 2, 2025/02/04 2025.

[21] B. Gajić *et al.*, 'Synergistic Integration of Polypyrrole, Graphene Oxide, and Silver Nanowires into Flexible Polymeric Films for EMI Shielding

Applications', *Molecules*, vol. 30, no. 21, p. 4221. doi: 10.3390/molecules30214221.

[22] B. Gajić *et al.*, 'Comparative Role of rGO, AgNWs, and rGO–AgNWs Hybrid Structure in the EMI Shielding Performance of Polyaniline/PCL-Based Flexible Films', *Molecules*, vol. 30, no. 24, p. 4693. doi: 10.3390/molecules30244693.

[23] M. Milenkovic *et al.*, 'Carbonized Apples and Quinces Stillage for Electromagnetic Shielding', *Nanomaterials*, vol. 14, no. 23. doi: 10.3390/nano14231882.

POSTER PRESENTATIONS

ТЕСЛИНИ ИНОВАЦИОНИ ДАНИ
TESLA INNOVATION DAYS
Belgrade, Serbia, April 7 - 8, 2025

DOI: 10.5937/TID25033G

ANALYSIS OF MAGNETIC FIELD LEVELS IN THE VICINITY OF THE TRANSMISSION POWER LINE TOWER AT THE LOCATION OF TRANSITION FROM OVERHEAD TO CABLE SECTION

Maja Grbić*, Dejan Hrvić, Katarina Maksić, Dragana Tomašević

Nikola Tesla Institute of Electrical Engineering, University of Belgrade, Republic of Serbia
* *maja@ieent.org*

Abstract

The paper analyses the levels of electromagnetic field in the vicinity of a 110 kV mixed transmission line tower, at the transition point between the overhead and underground sections. The aim of the research is to quantify the electromagnetic field levels near this tower and to compare them with the field levels on the overhead and underground cable sections of the line. The research encompasses two complementary approaches – field measurements and numerical modelling. The measurements of electromagnetic field were conducted under real conditions in the vicinity of the aforementioned tower, using appropriate measuring equipment. In addition to measurements, electromagnetic field calculations, based on power line modelling, are performed using specialized software. Simulations will provide a detailed insight into the spatial distribution of the electromagnetic field and enable comparisons with experimentally obtained results. The obtained results will provide an understanding of the differences in electromagnetic field levels around the tower compared to the levels in the overhead and underground cable sections of the transmission line. These results will be analysed in the context of current regulations regarding the protection of the general public from non-ionizing radiation. Besides analysing electromagnetic field levels, the paper also proposes measures to reduce the field levels around such towers and emphasizes the importance of proper planning and design of transmission lines to minimize the negative impacts of the electromagnetic field on the environment. The conclusions of the paper provide specific information on the characteristics of the electromagnetic field in the particular conditions of transition from an overhead to an underground cable section of the transmission line. They contribute to further research and the development of methods for reducing electromagnetic field in the vicinity of power lines.

Keywords: electromagnetic field, non-ionizing radiation, magnetic flux density, mixed transmission line, transmission power line.

1 Introduction

The paper is related to the topic of the protection of general public from non-ionizing radiation, i.e. low frequency electromagnetic field originating from the mixed transmission power line. The topic related to the influence of electromagnetic fields originating from power facilities and lines as well as possible mitigation techniques was analysed by several working groups [1–4]. Due to their length and proximity to residential areas, transmission lines are one of the most important sources of low frequency electromagnetic field in the environment. Knowing the levels of electric and magnetic fields in the vicinity of power lines is of great importance for planning the construction of new power lines near residential areas as well as for the construction of residential and other buildings near existing power lines. The levels of electric field strength and magnetic flux density in the vicinity of power lines have to be in compliance with the reference levels prescribed by international [5–7] and national [8–10] legislation. The levels of electric and magnetic fields near power lines are obtained by measurements and calculations. Measurements are carried out in accordance with the relevant standards [10–13], while calculations can be based on various methods. Different methods for the calculations of electric field strength and magnetic flux density are presented in [13–19]. The calculations in this paper are carried out using specialized software [20, 21]. The model used for calculations has to be previously verified in order to obtain reliable results which will be used for the assessment of compliance with the prescribed reference levels. The model can be verified by comparing the results with the results obtained by another software or by measurements. In this paper the method based on comparison with the measurement results was used.

The analysis in this paper is focused on the field levels near the 110 kV mixed transmission power line tower at the location of transition from overhead to cable section. In order to compare the results, the following three areas are analysed: 1) location at the overhead section of the line, 2) location at the cable section of the line and 3) location next to the tower where the

cables are descending to the ground. Since the results of electric field strength are relevant only for the overhead section of the line, the analysis is focused on magnetic field.

2 Legislation on protection from non-ionizing radiation

On the international level the reference levels for the protection of the general public from non-ionizing radiation are prescribed by the Recommendation 1999/519/EC [6] and guidelines published by International Commission on Non-Ionizing Radiation Protection (ICNIRP). The reference levels of exposure of the general public to power frequency (50 Hz) magnetic flux density, prescribed by [6], is set to 100 μT. This reference level is equal to the reference prescribed by the ICNIRP guidelines from 1998 [5]. In the ICNIRP guidelines from 2010 [7] the reference levels for power frequency (50 Hz) magnetic flux density is 200 μT. The Republic of Serbia fulfilled the requirements of [6] in 2009 by adopting the Law on Protection from Non-Ionizing Radiation [8] and several rulebooks. According to the Rulebook on Limits of Exposure to Non-Ionizing Radiation from 2025 [9], the reference levels for power frequency magnetic flux density are 40 μT for increased sensitivity areas and 100 μT for public areas. The term "increased sensitivity area" refers to residential areas, schools, homes, preschools, hospitals, tourist facilities etc.

3 Analysed situation of the 110 kV mixed transmission power line

Figure 1 shows the tower of the 110 kV mixed transmission power line at the transition point between the overhead and underground sections. Figures 2 and 3 show part of the tower where cable enters the ground. From the front, the cable is covered with a protective sheet, while from the back, direct access is possible.

Figure 1. The tower at the transition point between the overhead and underground sections

a) b)

Figure 2. Cables descending into the ground, shown from the front side (a) and from the back (b)

Figure 3 shows the location of the tower as well as four profiles (P_1–P_4) along which the calculations were carried out. The locations of the profiles are as follows:
P_1 – 20 cm from the center of the cable, inside the tower;
P_2 – 20 cm from the center of the side conductor of the cable line;
P_3 – away from the tower, above the route of the underground section of the cable, approximately perpendicular to the cable line route;
P_4 – away from the tower, perpendicular to the axis of the transmission line.

The profiles P_1 and P_2 are positioned next to the tower in order to analyse the influence of the cable descending to the ground. The profile P_3 is positioned away from the tower, above the route of the underground section of the cable, in order to analyse the contribution of that section only. The profile P_4 is also positioned away from the tower, below the overhead section of the line, in order to determine the contribution of the overhead section only. The profiles P_1–P_4 are located at the 1 m height above the ground, in accordance with the requirements of the standards [12, 13].

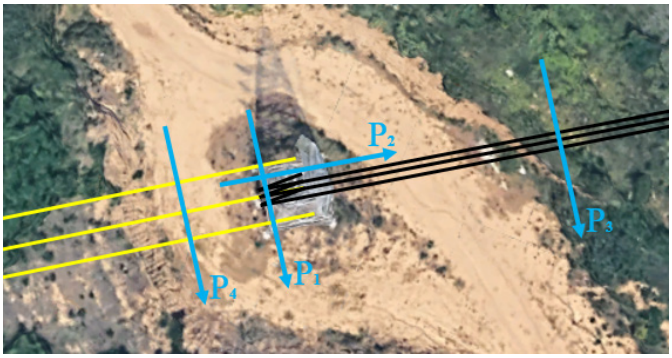

Figure 3. The location where the testing was conducted, showing the routes of the overhead and underground routes of the line, as well as the positions of the profiles

4 Results of magnetic field measurements and calculations

The analysis of the magnetic field levels is based on magnetic flux density measurements and calculations.

Measurements are carried out in accordance with the requirements of the standards [10–13]. During the testing, the rms values of magnetic flux density were measured isotropically, using magnetic field analyser connected to the isotropic probe for magnetic field measurements. The measuring system fulfils the requirements of the standard [11].

The calculations are carried out using specialized software [20, 21], based on Partial Element Equivalent Circuit (PEEC) method.

Figure 4 shows the geometry of the phase conductors and ground wire at the overhead section of the line next to the tower.

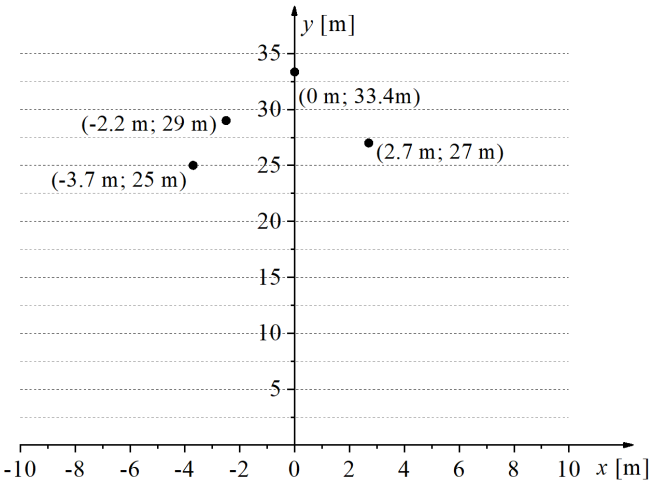

Figure 4. Geometry of the line near the tower

The type of the cable line is 3 x (XLPE 300/95 mm^2) and its maximum current is 481 A. The type of the phase conductors at the overhead section is ACSR 240/40 mm^2. Its maximum current in the winter period is 880 A. Since the maximum current of the entire power line is limited on 481 A the calculations are carried out for this value.

The magnetic flux density measurements are carried out at the profiles P_1 and P_4. During the measurements the power line current was I_m = 107 A. The magnetic flux density calculations are carried out along the profiles P_1–P_4 for the power line current at the time of measurements (I_m = 107 A) and for the maximum power line current (I_{max} = 481 A). The obtained results are presented in Figures 5–8.

Figures 9 and 10 show the magnetic flux density results obtained by calculations at the planes located near the tower at the height of 1 m above the ground. The dimensions of the planes are 2 m x 1 m. The calculations were made for the maximum current intensity.

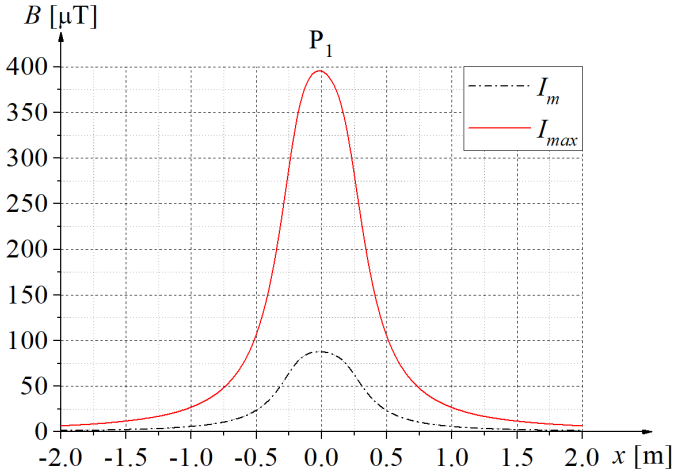

Figure 5. Magnetic flux density values obtained by calculations along the profile P_1 for maximum current (481 A) and the current during measurements (107 A)

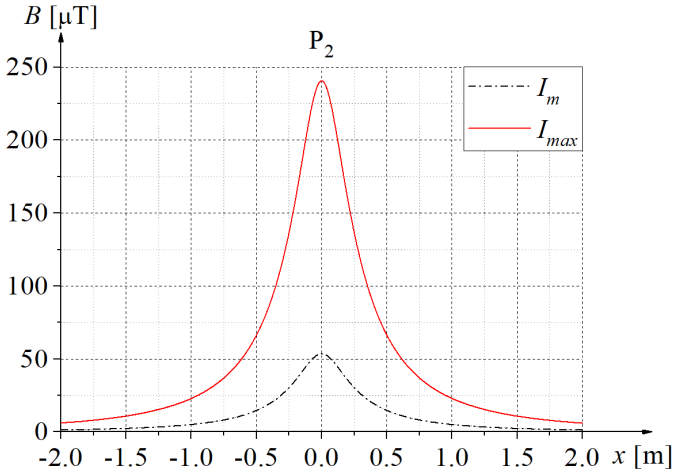

Figure 6. Magnetic flux density values obtained by calculations along the profile P_2 for maximum current (481 A) and the current during measurements (107 A)

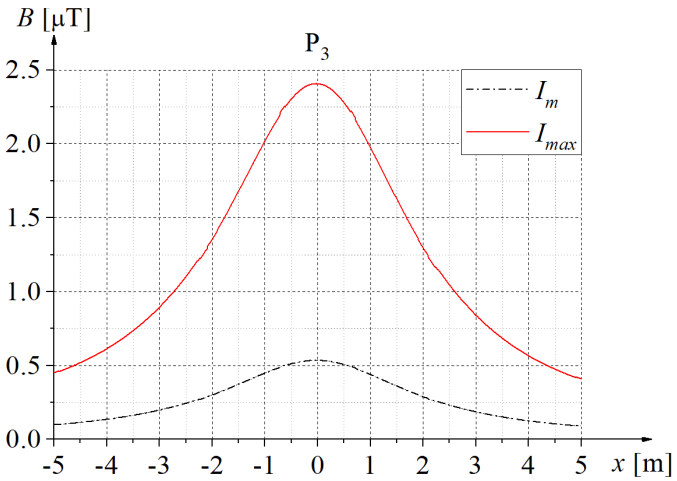

Figure 7. Magnetic flux density values obtained by calculations along the profile P_3 for maximum current (481 A) and the current during measurements (107 A)

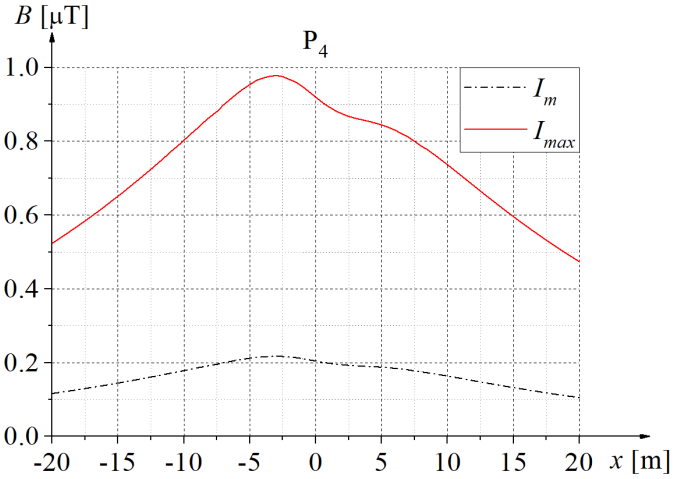

Figure 8. Magnetic flux density values obtained by calculations along the profile P_4 for maximum current (481 A) and the current during measurements (107 A)

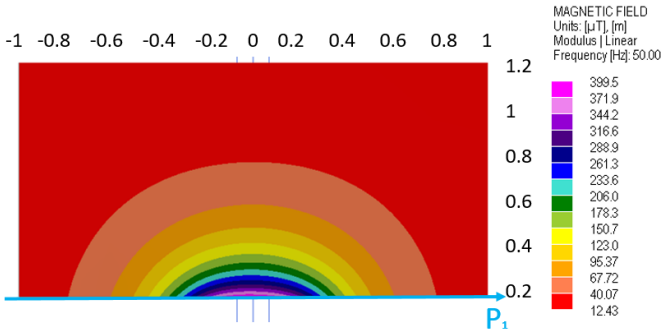

Figure 9. Values of magnetic flux density obtained by calculations on the plane located at the height of 1 m above the ground, on the back of the cable

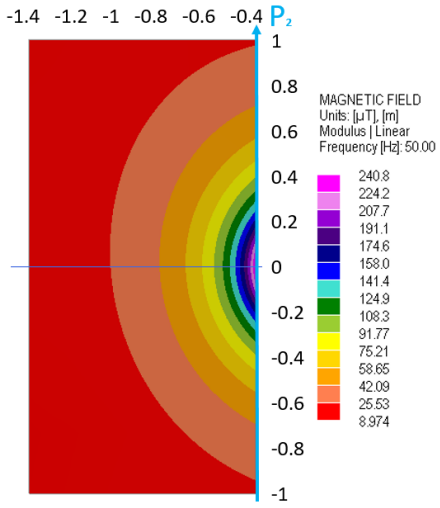

Figure 10. Values of magnetic flux density obtained by calculations on the plane located at the height of 1 m above the ground, on the side of the cable

Table 1 shows the maximum values of magnetic flux density along different profiles obtained by measurements and calculations for the current present at the time of measurements.

Table 1. Maximum magnetic flux density values (B_m) obtained for I_m = 107 A

I_m = 107 A	Maximum values of magnetic flux density [μT]			
	P_1	P_2	P_3	P_4
Measurements	88	/	/	0.26
Calculations	89	55	0.55	0.22

From the results given in Table 1 it can be concluded that there is an agreement between the results obtained by measurements and calculations along the profiles P_1 and P_4. Since the power line model used for calculations is verified it can be used for calculating maximum values of magnetic flux density which occur in the case when the power line current is equal to the maximum current.

Table 4 shows the maximum values of magnetic flux density along different profiles obtained by calculations for the power line maximum current.

Table 2. Maximum magnetic flux density values (B_{max}) obtained for I_{max} = 481 A

I_{max} = 481 A	Maximum values of magnetic flux density [μT]			
	P_1	P_2	P_3	P_4
Calculations	399.5	240.8	2.45	0.99

From the presented results it can be concluded that the highest values of magnetic flux density are obtained along the profiles P_1 and P_2, which are located near the tower, i.e. next to location where the cable enters the ground. These results are obtained due to the proximity of the profiles to the cable. The results obtained at profiles P_1 and P_2 for the maximum current exceed the reference level of 100 μT prescribed by [9] for public areas as well as by [5, 6]. These results also exceed the reference level of 200 μT prescribed by [7]. The results obtained along the profiles P_3 (underground cable section) and P_4 (overhead section) are significantly lower compared to the results along the profiles P_1 and P_2. The results obtained along the profiles P_3 and P_4 are significantly lower than the reference levels of 100 μT and 200 μT even in the case of the maximum power line current. The lowest values of magnetic flux density are obtained along the profile P_4 which correspond to the overhead section.

The levels of magnetic field in the vicinity of the tower, i.e. near the cable can be reduced by placing a conductive shield around it [22]. Another possibility is to place a fence around the tower at a certain distance in order to prevent the population from getting close to the cable and entering the area where the magnetic field values exceed the prescribed reference levels.

5 Conclusion

The levels of magnetic field which occur in the vicinity of the 110 kV mixed transmission power line are analysed in the paper. The results show that significantly higher values are obtained at the location next to the tower where the cables are

descending to the ground compared to the values obtained at the overhead section and underground cable section of the power line. The values obtained at the location where the cables enter the ground, at the distance of 20 cm from the cables, can exceed the reference levels prescribed by [5, 6, 9]. These magnetic field levels can be reduced by applying the shielding system, i.e. placing the conductive shield around the cables. Another possibility is to place a fence around the cable to prevent the population from entering the area with high magnetic field values.

6 Acknowledgements

This work was supported in part by the Ministry of Science, Technological Development and Innovation of the Republic of Serbia under the Contract on the realization and financing of the scientific research work of research and innovation organizations in 2025.

7 References

[1] Technical guide for measurement of low frequency electric and magnetic fields near overhead power lines, CIGRE Working Group C4.203, 2009.

[2] Mitigation techniques of power frequency magnetic fields originated from electric power systems, CIGRE Working Group C4.204, 2009.

[3] Characterisation of ELF magnetic fields, CIGRE Working Group C4.205, 2007.

[4] Responsible management of electric and magnetic fields, CIGRE Working Group C3.19, 2020.

[5] International Commission on Non-Ionizing Radiation Protection, "ICNIRP guidelines for limiting exposure to time-varying electric, magnetic, and electromagnetic fields (up to 300 GHz)", Health Phys., vol. 74, No. 4, 1998, pp. 494–522.

[6] 1999/519/EC: "Council Recommendation of 12 July 1999 on the limitation of exposure of the general public to electromagnetic fields (0 Hz to 300 GHz)", OJ L, L 199, 1999, pp. 59–70.

[7] International Commission on Non-Ionizing Radiation Protection, "ICNIRP guidelines for limiting exposure to time-varying electric and magnetic fields (1 Hz – 100 kHz)", Health Phys., vol. 99, no. 6, 2010, pp. 818–836.

[8] "Law on protection from non-ionizing radiation", Official Gazette of Republic of Serbia No. 36/09, May 15, 2009.

[9] "Rulebook on limits of exposure to non-ionizing radiation", Official Gazette of Republic of Serbia No. 16, February 26, 2025.

[10] EN 50413: "Basic standard on measurement and calculation procedures for human exposure to electric, magnetic and electromagnetic fields (0 Hz – 300 GHz)", 2019.

[11] IEC 61786: "Measurement of DC magnetic, AC magnetic and AC electric fields from 1 Hz to 100 kHz with regard to exposure of human beings – Part 1: Requirements for measuring instruments", 2013.

[12] IEC 61786: "Measurement of DC magnetic, AC magnetic and AC electric fields from 1 Hz to 100 kHz with regard to exposure of human beings – Part 2: Basic standard for measurements", 2014.

[13] EN 62110: "Electric and magnetic field levels generated by AC power systems – Measurement procedures with regard to public exposure", 2009.

[14] Power lines: Demonstrating compliance with EMF public exposure guidelines: A voluntary code of practice. Government of the UK, Department of Energy & Climate Change, London, UK, 2012.

[15] Turajlić, E., Mujezinović, A., Alihodžić, A.: "A novel method based on PSO algorithm and ANN for magnetic flux density estimation near overhead transmission lines", J. Electr. Eng., 2024, vol. 74, pp. 399-410.

[16] Alihodžić, A., Mujezinović, A., Turajlić, E.: "Artificial neural network-based method for overhead lines magnetic flux density estimation", J. Electr. Eng., 2024, vol. 75, pp. 181-191.

[17] Grbić, M., Pavlović, A.: "Determining the zone of influence of transmission overhead power lines from the aspect of non-ionizing radiation", Proc. of the 6th International RAD Conference, 2018, vol. 3, pp. 52–57.

[18] Grbić, M., Mikulović, J., Salamon, D.: "Influence of measurement uncertainty of overhead power line conductor heights on electric and magnetic field calculation results", Int. J. Electr. Power Energy Syst., (2018), 2017, vol. 98, pp. 167–175.

[19] Grbić, M., Salamon, D., Mikulović, J.: "Analysis of influence of measuring voltage transformer ratio error on single-circuit overhead power line electric field calculation results", Electr. Power Syst. Res., 2018, vol. 166, pp. 232–240.

[20] XGSLab User's Guide, SINT Ingegneria Srl, 2025.

[21] XGSLab Tutorial XGSA_FD, SINT Ingegneria Srl, 2025.

[22] Grbić, M., Canova, A., Giaccone, L., Pavlović, A., Grasso, S.: "Mitigation of low frequency magnetic field emitted by 10/0.4 kV substation in the school", Int. J. Numer. Model.: Electron. Netw. Devices Fields.

ТЕСЛИНИ ИНОВАЦИОНИ ДАНИ
TESLA INNOVATION DAYS
Belgrade, Serbia, April 7 - 8, 2025

DOI: 10.5937/TID25038O

ANALYSIS OF THE CONDUCTIVE COUPLING BETWEEN 220/66/11 KV SUBSTATION AND NEARBY PIPELINE DURING EARTH FAULT

Stefan Obradović[1], Maja Grbić[1], Goran Lepović[2*]

[1] *Nikola Tesla Institute of Electrical Engineering, University of Belgrade, Republic of Serbia*
[2] *Siemens doo Belgrade*
[*] *stefan.obradovic@ieent.org*

Abstract

The aim of this paper is to analyse the conductive coupling between the earthing grid of the 220/66/11 kV substation and the nearby underground pipeline, under fault conditions. It evaluates the potential risks to personnel safety, pipeline integrity, and outlines necessary mitigation measures. The pipeline passes approximately 40 m from the substation, which is within the proximity threshold of 150 m specified by the EN 50443 standard for considering conductive coupling. The study is focused on analysing the effects of a single-phase-to-earth fault at the substation and its impact on the pipeline. Under fault conditions, high voltages can appear between the pipeline and surrounding soil, which can lead to coating stress voltages and touch voltages. To evaluate conductive interference, the primary concern is the pipeline voltage to earth. For personnel protection, the interference voltage shall not exceed the values stated in EN 50443 and IEEE 80. The latter specifies a stricter limit for touch voltage of 235 V for a fault duration of 0.35 s. For pipeline protection, the interference voltage shall not exceed 2000 V, both for the pipeline system relative to earth and across insulating joints. Coating stress voltages were calculated along the pipeline, with results showing that the voltage in the vicinity of the substation is just below the 2000 V limit as defined by EN 50443. The calculated voltages across the insulating joints are below the 2000 V threshold, as specified by EN 50443. Touch voltages, which can pose a significant safety risk to personnel, were calculated along the pipeline. In the vicinity of the substation, touch voltage values exceed the IEEE 80 limit of 235 V. The study identified a zone where touch voltages exceed this threshold, with a maximum of 2006 V. This zone corresponds to the locations of above-ground appurtenances where the risk of electric shock is highest. To address the risk posed by touch voltages, the study recommends insulation of the operation location with sufficient insulating material. A surface layer of at least 80 mm of insulating material with a specific electrical resistivity of 10,000 Ωm is required to mitigate the risks effectively. This insulation shall ensure that the appurtenances can only be touched by standing on the insulating layer, thus eliminating the risk of electric shock. After applying the recommended surface layer, touch voltages were recalculated, and the results showed that they fall below the 235 V threshold, ensuring personnel safety. The results underline the need for regular monitoring and implementation of safety measures to protect both personnel and pipeline infrastructure from the hazardous effects of fault-induced conductive interference.

Keywords: conductive coupling, earthing grid, underground pipeline, earth fault, touch voltage, coating stress voltage, mitigation measure.

1 Introduction

High voltage power facilities and lines may impact their environment by emitting electromagnetic field [1, 2] as well as through electromagnetic interference with the nearby objects. In this paper the impact of a high voltage substation on a nearby pipeline is analysed. The aim of the paper is to present and interpret the results of the analysis of conductive coupling between earthing grid of 220/66/11 kV GIS substation and nearby crude oil pipeline. Electromagnetic interference, in general, is present between power facilities and adjacent metallic structures during normal operating conditions and faults. It consists of an inductive, conductive, and capacitive component. Underground pipelines are not influenced by capacitive component, because of the screening effect of the earth against electric fields. Aerial and underground pipelines that run parallel to or in close proximity to transmission lines or cables are subjected to inductive interference caused by the time-varying magnetic fields produced by the transmission line currents, which results in induced voltages in the pipeline. The conductive component arises only in fault conditions and, specifically, in cases where the pipeline is located near the faulted structure. In this particular case, the underground pipeline is running in the vicinity of a high-voltage substation, and it is assumed that the pipeline is not running parallel with any power line leaving the substation. Therefore, only conductive interference between the pipeline and earthing grid of the substation, in case of a fault in the substation, is analysed.

The calculations in the paper are carried out in accordance with [3-8] by using a specialized software [9-10].
An underground DN650 pipeline is installed between two valve stations. The pipe is buried at a depth of 1.5 m. The total length of the pipeline is around 24 km. At the length of about 19 km, the pipeline runs close to 220/66/11 kV GIS substation, at a distance of 40 m approximately. According to standard EN 50443 [3], conductive coupling between an earthing grid of a substation and pipeline shall be considered in case when the distance is less than 150 m. Therefore, it is necessary to analyse the conductive coupling between the pipeline and the substation, for the case when a single-phase-to-ground fault occurs at the substation, as well as the effects of interference.
Protection of both personnel and long-term pipeline damage will be considered. The primary concern for personnel protection under fault conditions are touch voltages at or near appurtenances or across the insulating joints. Under fault conditions, high voltages can appear between the pipeline and the surrounding soil. This is defined as a coating stress voltage. If the coating stress voltage becomes too high, the coating can break down in that area. Interference voltage can also occur across an insulating joint. Obtained values of coating stress voltage and touch voltages along the pipeline are compared with the limits prescribed by EN and IEEE standards.

2 Input data

In order to analyse the effect of conductive coupling, it is necessary to model the electrical and geometric characteristics of the underground pipeline and the earthing grid of the substation, as well as to form the appropriate soil model. An underground pipeline is installed between two valve stations. The pipeline is buried at a depth of 1.5 m, except near the substation, where the actual burial depth is taken from the crossing profile, with a maximum depth of 12 m.

In Table 1, the geometrical and electrical characteristics of the underground pipeline are given. It is assumed that the pipeline is not grounded on the entire length. At both ends of the pipeline, insulating flanges are installed. The dielectric strength of installed joints is 2.5 kV. The exact locations of pipe appurtenances are not known but can be assumed periodically at 2 km intervals.

In Figure 1 the substation earthing grid layout is shown. The earthing grid is composed of horizontal copper electrodes, with 2 x 240 mm^2 cross-section, and of vertical earthing rods, with a length of 3 m. It is assumed that the earthing grid is laid at a depth of 1 m. Parameters of soil, in the vicinity of the substation, are given in Table 2. The parameters given in Table 2 are adopted from measurements taken at the substation location.

In order to calculate conductive coupling between the earthing grid of the substation and pipeline, it is necessary to determine the portion of fault current returning through the earth. When a ground fault occurs, the zero-sequence fault current returns through alternate paths such as neutral conductors, overhead earth wires, and metallic cable shields. The ground sources are the grounded wye–connected windings of power transformers, generator grounds, shunt capacitors, etc. The ground potential rise is equal to the product of the substation ground grid impedance and the portion of the total fault current that flows through it. The potential of the soil in the vicinity of the substation grounding will increase relative to the potential of the remote earth. Part of the ground potential rise is transferred to the sheath of the pipeline in the event of a fault to the ground.

Table 1. Electrical and geometrical properties of the pipeline for calculation purposes

Pipeline diameter	66 cm
Pipeline thickness	1.27 cm
Pipeline covering layer thickness	0.5 cm
Pipeline burial depth	1.5 cm
Pipeline material	Steel
Pipeline covering layer material	Polyethylene
Pipeline electrical resistivity	$5 \cdot 10^{-8}$ Ωm
Pipeline relative permeability	100
Covering layer electrical resistivity	$1 \cdot 10^{14}$ Ωm

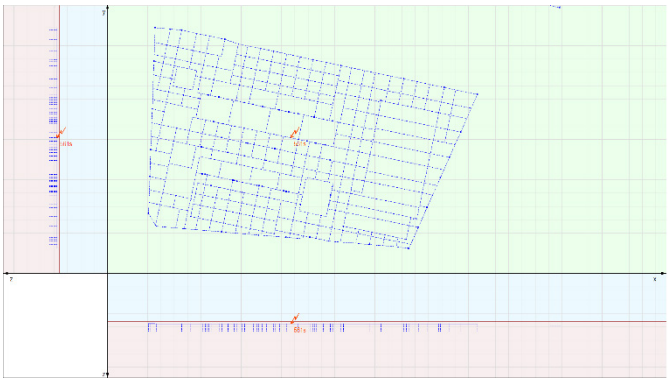

Figure 1. Substation earthing grid

Table 2. Soil parameters

Soil model	Soil resistivity [Ωm]
Uniform	128

Earth wires of overhead lines and metal sheaths of underground cable participate in carrying fault currents returning to the earth. They take over a part of the earth's current of the corresponding circuit. The extent of this effect is described by the reduction factor. The reduction factor r for an earth wire of a 3-phase overhead line is the ratio of the return current in the earth to the sum of the zero-sequence currents of the 3-phase circuit, as given in formula (1).

$$r = \frac{I_E}{3 \cdot I_0} \tag{1}$$

where the marks denote the following:
- I_E - earth return current;
- $3 \cdot I_0$ - sum of zero sequence currents.

The same definition is relevant to the reduction factor r of an underground cable with a metallic sheath, screen, armouring, or an enveloping steel pipe. Instead of the current in the earth wire I_{EW} the current in the metal sheath has to be used. The reduction factor can be calculated on the basis of the self-impedances of the phase conductors and the earth wire and the mutual impedance between phase conductors and earth wire.

The value of the single phase to ground fault current, at substation, is given in Table 3. Four 220 kV cables are leaving the substation, and there are no overhead lines. Therefore, to determine the earth's return current, it is necessary to calculate the reduction factor of those cables. Since the geometrical end electrical information about HV cables is not known, the value of the reduction factor will be adopted. According to standard EN 50522 [4], a value of 0.2 is adopted in Table 3. Fault clearing time is 0.35 s.

Table 3. The substation ground fault details at 220 kV voltage level

Fault current [kA]	Earth return current [kA]	Fault clearing time [s]
39.5	7.9	0.35

3 Considerations

In order to evaluate the acceptability of a conductive interference in the event of a fault at the substation, produced between an earthing grid of the substation and a nearby pipeline, it is necessary to select the involved interference effects to be considered. The effects of conductive interference to consider are the following:

- danger to persons who come in direct contact or contact through conductive parts with the metallic pipeline system or with the connected equipment;
- damage to the pipeline or to the connected equipment.

To assess interference results, the voltage to earth of the pipeline and the voltage difference on the insulating joints will be evaluated. According to standard EN 50443 [3], for the fault conditions, the interference voltage (r.m.s. value) of the pipeline system versus earth or across the insulating joints at any point normally accessible to electrically instructed persons shall not exceed the values given in Table 4. Limits given in Table 4 refer to instructed persons with common clothing, without particular individual protection means other than shoes with an insulating resistance not less than 3,000 Ω. This criterion applies to instructed persons. For non-instructed persons, a stricter criterion is specified by the IEEE 80 standard [8]. The value of 235 V is used for a fault clearing time of 0.35 s.

Table 4. Limits for interference voltage related to danger to (electrically) instructed persons

Fault duration t [s]	Interference voltage (r.m.s. value)
$t \leq 0.1$	2,000
$0.1 < t \leq 0.2$	1,500
$0.2 < t \leq 0.35$	1,000
$0.35 < t \leq 0.5$	650
$0.5 < t \leq 1$	430
$1 < t \leq 3$	150
$t > 3$	60

Regarding limits related to damage to the pipeline system, according to EN 50443 [3], the interference voltage (r.m.s. value) between the metallic pipeline system and the earth at any point of the pipeline system, or the interference voltage (r.m.s. value) between any element of the electric/electronic equipment connected between the metallic pipeline and the earth, shall not exceed 2,000 V. Also, the voltage difference (r.m.s. value) across an insulating joint shall not exceed 2,000 V.

4 Coating stress voltage

Based on the input data, a model of the earthing grid of the substation and a model of the pipeline are formed. The model of the earthing grid is shown in Figure 1, and the model of the pipeline is shown in Figure 2. The pipeline layout near the substation is shown in Figure 3.

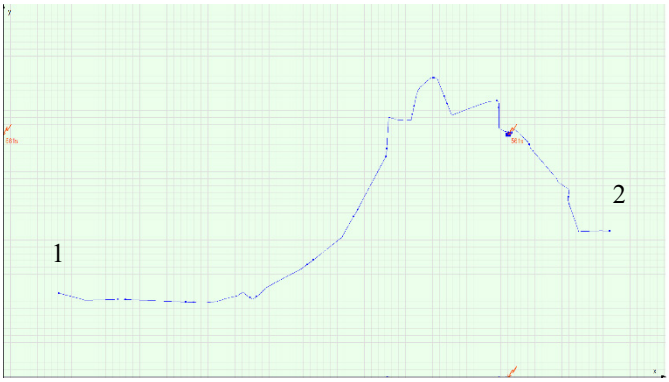

Figure 2. Pipeline layout

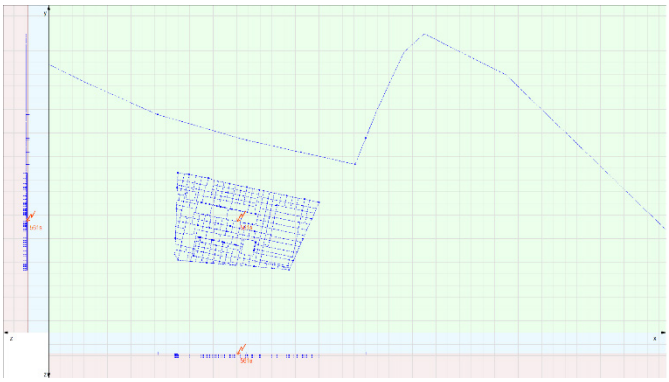

Figure 3. Pipeline layout near the earthing grid

For the calculation of conductive interference, a portion of the fault current, given in Table 3, is used. Coating stress voltage on the pipeline and touch voltages, along the pipeline, are calculated.

Coating stress voltage results are shown in Figures 4, 5, and 6. In Figure 4, coating stress along the pipeline, as a function of distance from the far end (1) of the pipeline, is represented. In the figure, the limit for coating stress voltage, according to EN 50443 [3], is given. In Figures 5 and 6, covering stress voltage distribution near the substation is given. From these figures, it can be concluded, that the coating stress voltage on the portion of the pipeline in the vicinity of the substation, is just below the 2,000 V limit.

The voltages across insulating joints, located at both ends of the pipeline, are given in Table 5. The positions of insulating joints are shown in Figure 2. The voltages are below 2,000 V.

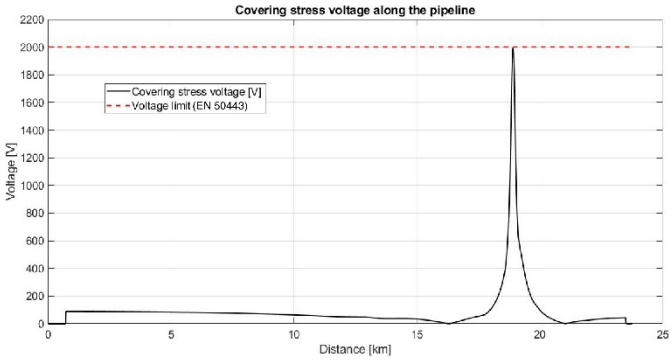

Figure 4. Coating stress voltage on the pipeline

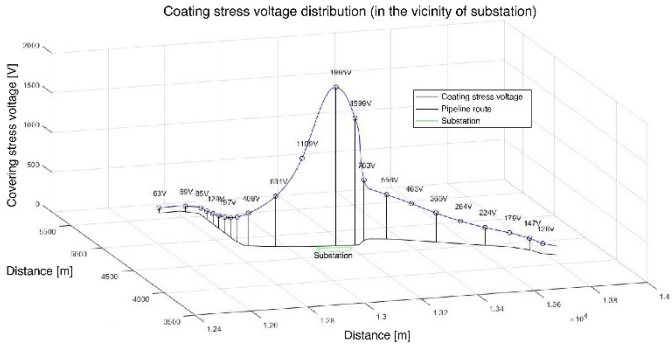

Figure 5. Coating stress voltage distribution

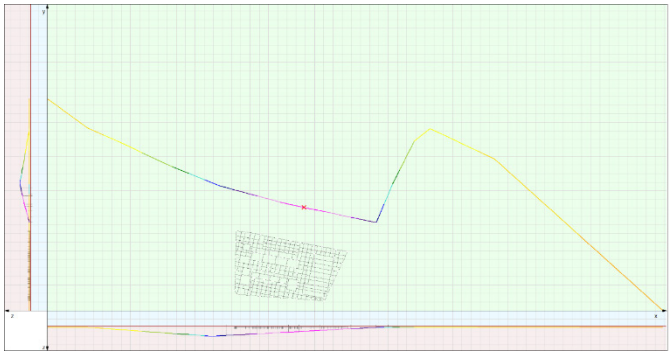

Figure 6. Coating stress voltage on the pipeline near substation

Table 5. Voltages across insulating joints

Insulating joint position	Voltage across insulating joint [V]
Pipeline end 1	89
Pipeline end 2	45

5 Touch voltage

Touch voltage distribution, in the vicinity of the substation, is given in Figures 7 and 8. For the calculation of the touch voltages along the pipeline, a distance of 2 m from the pipeline is assumed.

In Figure 7, two zones along the pipeline are given. The green zone, marked in the figure, along the pipeline, represents a zone where touch voltages are below the limit of 235 V, according to IEEE 80 [8]. The yellow zone indicates the section of the pipeline where touch voltages exceed the permissible limit of 235 V. The location of this zone is shown in Figure 7. The maximum value of touch voltage in the yellow zone is 2,006 V. However, touch voltages only exist in places on the pipeline where above-ground appurtenances are present. The same applies to the yellow zone, where touch voltages above the limit are present. Mitigation measures are required for all appurtenances located in the yellow zone shown in Figure 7.

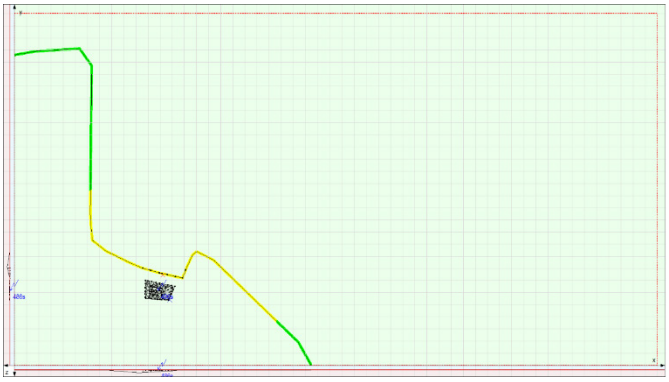

Figure 7. Touch voltage on the pipeline

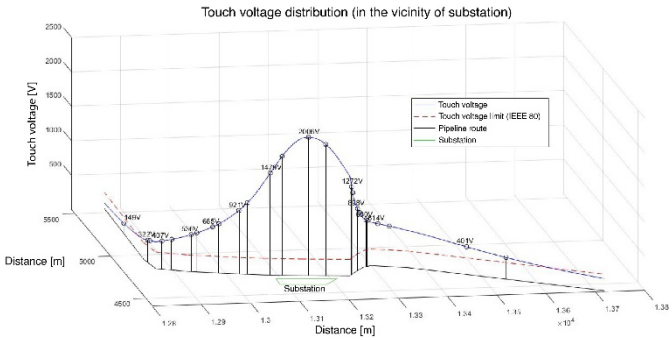

Figure 8. Touch voltage distribution near the substation

Voltages across insulating joints, given in Table 5, are below the limit of 235 V.

6 Mitigation measures for touch voltages

One possible measure to mitigate touch voltages around above-ground appurtenances is to insulate the operational area using an appropriate insulating material, as illustrated in Figure 9. The insulating layer must be large enough to prevent any contact with the above-ground appurtenances from outside the insulated area. Mitigation measures are required for all appurtenances located within the yellow zone shown in Figure 7. According to the results of calculations carried out in line with IEEE 80 [8], an additional surface layer with a thickness of 80 mm and a specific electrical resistivity of 10,000 Ωm is required for the location with the highest calculated touch voltage. As the exact locations of the appurtenances are not known, the worst-case location has been assumed.

Touch voltage distribution, in the vicinity of the substation, after adding the surface layer, is given in Figure 10. It can be concluded that after adding the surface layer, the touch voltage on the portion of the pipeline in the vicinity of the substation is below the 235 V limit.

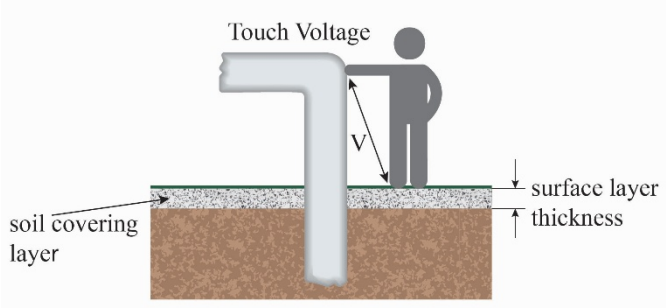

Figure 9. Touch voltage mitigation measure through the addition of a high resistivity surface layer

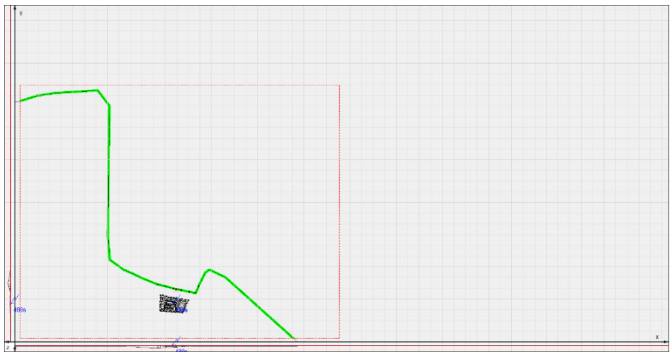

Figure 10. Touch voltage on the pipeline after mitigation measures

7 Conclusion

Calculations of interference effects due to the conductive coupling between the earthing grid of the 220/66/11 kV substation and the nearby underground pipeline, in the event of a fault in the substation, were carried out. The results, covering stress voltages on the pipeline and touch voltages near the pipeline, were then compared with the corresponding limits.

The calculations show that the covering stress voltage along the entire length of the pipeline remains below the limit specified by EN 50443. However, touch voltages near the substation exceed the limit defined by IEEE 80. Voltages across insulating joints are within the permissible limits for both touch voltage and voltage difference across the joints.

Touch voltages above the 235 V limit occur along a section of the pipeline. These voltages only appear where above-ground appurtenances are present, with a maximum touch voltage of 2,006 V. To mitigate touch voltages around above-ground appurtenances, the specific electrical resistivity of the surface soil can be increased by applying an insulating layer of asphalt or crushed stone with a minimum thickness of 80 mm and a resistivity of 10,000 Ωm. The insulating layer must be sufficiently large to prevent contact with the appurtenances from outside the layer. Mitigation measures are required for all appurtenances located within the yellow zone depicted in Figure 9.

8 Acknowledgements

This work was supported in part by the Ministry of Science, Technological Development and Innovation of the Republic of Serbia under the Contract on the realization and financing of the scientific research work of research and innovation organizations in 2025.

9 References

[1] M. Grbić, J. Mikulović, D. Salamon, “Influence of Measurement Uncertainty of Overhead Power Line Conductor Heights on Electric and Magnetic Field Calculation Results”, Int. J. Electr. Power Energy Syst., vol. 98, (2018), 2017, pp. 167–175.

[2] M. Grbić, D. Salamon, J. Mikulović, “Analysis of Influence of Measuring Voltage Transformer Ratio Error on Single-Circuit Overhead Power Line Electric Field Calculation Results”, Electr. Power Syst. Res., vol. 166, 2018, pp. 232–240.

[3] EN 50443:2011: ‘Effects of electromagnetic interference on pipelines caused by high voltage a.c. electric traction systems and/or high voltage a.c. power supply systems’, 2011.

[4] EN 50522:2022: ‘Earthing of power installations exceeding 1 kV a.c.’, 2022.

[5] IEEE 2746:2020: ‘IEEE Guide for Evaluating AC Interference on Linear Facilities Co-Located Near Transmission Lines’, 2020.

[6] CIGRE, Technical Brochure 095: ‘Guide on the influence of high voltage AC power systems on metalic pipelines’, 1995.

[7] ITU-T: K.68:2008: ‘Management of electromagnetic interference on telecommunication systems due to power systems and operator’s responsibilities’, 2008.

[8] IEEE 80:2013: ‘Guide for Safety in AC Substation Grounding’, 2013.

[9] XGSLab User’s Guide, SINT Ingegneria Srl, 2024.

[10] XGSLab Tutorial XGSA_FD, SINT Ingegneria Srl, 2024.

ТЕСЛИНИ ИНОВАЦИОНИ ДАНИ
TESLA INNOVATION DAYS
Belgrade, Serbia, April 7 - 8, 2025

DOI: 10.5937/TID25043A

INNOVATIVE INSTRUMENT DESIGN FOR SYSTEMS WITH VARYING FREQUENCY INPUTS

***Boris Antić*[1]**

[1]*Smart Grid Solutions doo Novi Sad, Serbia*

Abstract

The paper provides some practical aspects of frequency multiplication applied to the synchronization of power grid instruments operating at unknown frequency or in a regime with a constant small frequency drifts. The circuit that realizes the multiplication is intended to replace the device's internal clock and to guarantee fixed pre-defined (programmable) number of samples per period of the input signal. This prevents spectrum leakage and other issues associated with spectrum calculations from time samples using common time-frequency transformations. Consequently, the architecture of the device implementing this solution can be simplified through elimination of digital circuits for various filtering and numerical corrections. Two possible architectures for the realization of this device are presented and the restrictions necessary to ensure adequate positioning of harmonics along the frequency axis are shown.

Keywords: Power quality, Varying frequency, Power instrumentation, VLSI.

1 Introduction

Frequency determining devices implemented in power instrumentation are usually able to determine frequency and phase information for signals and are utilized in a large variety of communication and power systems, miniaturized electric and optical spectrometers [1] as well as consumer electronic devices using AI-based PCBs [2] or low-power VLSI [3]. They may also be applied for synchronizing multiple signals at varying frequencies to a preset frequency, as is the case in power networks, where a fixed fundamental frequency is often assumed. Examples can be found in [4] with the case of assumed fixed frequency of the power network, and in [5], where a concrete DSP performance is analysed against harmonic analysis for power quality control. In most applications restricted to environments with well-established nominal frequencies, the architecture of the chip usually assumes a known (nominal) value of the fundamental frequency f_0 [6]. However, when dealing with precise spectral (harmonic) measurements based on Fourier expansion from signal samples, it is important to recognize the challenge of the unknown fundamental frequency of the measured signal whenever it exhibits small but constant fundamental frequency drifts. Additional issues such as temperature variations and aging of the VLSI chip can introduce additional inconsistency in synchronization between the input signals and the device internal clock.

In [7] the pitfalls of the FFT are analysed and in [8] the drawbacks of DTF implemented in a concrete DSP are shown. In both cases, alternatives are proposed. When a VLSI chip fails to ensure adequate and constant number of samples per each period of the signal, the original assumption of the "known" fundamental frequency causes numerous errors. Firstly, all spectral components will assume incorrect positions along the frequency axis compared to their actual analogue values.

Let a_i and b_i represent spectral component of the order i. Small drift Δf of the fundamental frequency from the nominal value f_0 will affect perceived positions of the Fourier's coefficients affecting each higher harmonic more severely, as is illustrated in Fig. 1.

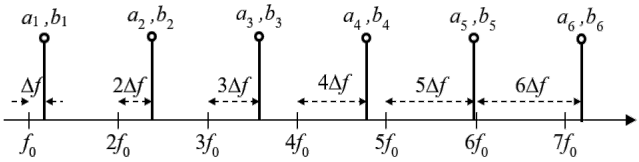

Figure 1. Incorrect placement of spectrum components due to unknown variations Δf of the nominal value of the fundamental frequency f_0

This incorrect placement of energy along the frequency axis varies in time and it is impossible to predict during the instrument design phase.

Secondly, the drift Δf can lead to the leakage effect or undesired transfer of energy between spectral components due to the inability of the Fourier expansion to compensate for any discrepancy in assumed and actual fundamental frequency. In extreme cases, it can cause phantom spectral components to

appear or actual components to disappear from the spectrum. This is shown in Fig. 2.

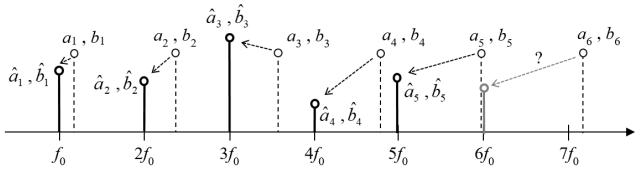

Figure 2. Redistribution of energy among actual (a_i, b_i) and pre-positioned $(\hat{a}_i, \hat{b}_i)$ spectral components due to incorrect sampling of the input signal

Knowing the exact fundamental frequency and uniformly sampling with identical number of samples over each period are the two prerequisites for the elimination of the measurement error due to the spectrum leakage. In order to achieve this it is necessary to adapt to small frequency variations e.g. by generating the exact multiple of the fundamental frequency of the measured signal and dynamically tuning the internal clock of the instrument to that frequency. No present known VLSI architecture allows for such flexible solution.

One possible approach to address the issue is to use analogue frequency sweeping circuits to measure the true spectrum of the signal. Besides being an expensive solution, this approach requires very fast analogue circuitry and it extends beyond the intended scope of this article. Another option is to assume the known fundamental frequency, ignore any variations and attempt to compensate the error with numerical post-processing of measurement results [9]. This is a viable option as long as the numerical computation error does not exceed the error caused by the frequency drift. Finally, the most elegant solution is to create a frequency multiplier necessary to overcome the problems of spectrum leakage. This can be realized in several ways, which are briefly explained below.

In [10] one can find a possible workaround using of a series of switching (rectifying) semiconductor elements, each of which doubles the input frequency. This usually creates short, but unstable no-signal zones corresponding to non-conducting intervals around zero-crossing points. Depending on the noise level, this can affect the stability of each element in a series and accumulate error when high multiples are required. Another solution is the utilization of non-linear elements, such as step recovery diodes or class C transistors to generate higher harmonics [11]. The drawback is that the energy levels of harmonics of very high orders are usually too low and contain an unacceptable amount of noise. Additionally, they require relatively complex and expensive digital FIR filters to remove all undesired multiples of the fundamental frequency.

A further known approach is provided by analogue PLLs (Phase Locked Loops) with the voltage control oscillator set to the multiple of the input frequency. Frequency multiplication or synthesis through PLL means at least one entire period delay to any change at the input. In [12] one can find disclosed a special realization of a system and method to detect the fundamental frequency of an electric input signal using a feedback control loop including a phase error detector, a loop controller, and a digitally controlled oscillator.

Another known technique is a chip design with arithmetical multiplication of the measured frequency and synthesis of an output signal corresponding to the result of that multiplication. These solutions are relatively complex and consume many resources to be integrated into less hardware demanding measurement devices e.g. such as compact handheld devices. For example [13] discloses a method and apparatus for clocking the chip at a frequency which is always a constant integer multiple of the fundamental frequency of the input analogue signal. However, the value of that multiplication is limited to a very small number due to the number of required operations. In addition, worthy of noting is that this solution requires a separate circuit to provide clock for the measurement circuit. These integrated frequency multipliers have limited capabilities of multiplication factors up to 100, while e.g. in spectrometers or power grid instruments it is required that the frequency is multiplied by a factor of several thousand or hundreds of thousands. Most frequency multipliers are produced for microwave RF modules and they cover the range from 100 MHz to 24 GHz, thus cannot be applied to low frequency multiplication.

In this paper, we present possible realization of a much simpler low-cost solution for frequency multiplication by any given factor. The circuit is based on [14] and in the following sections, its potential impact on the design of future VLSI architectures is considered.

2 Novel Approach to Instrument Clocking

2.1 Universal Frequency Multiplying Circuit

A generic universal solution for frequency multiplication can be found in [14]. This concept yields a concrete realization of digital circuitry depicted in Fig. 3.

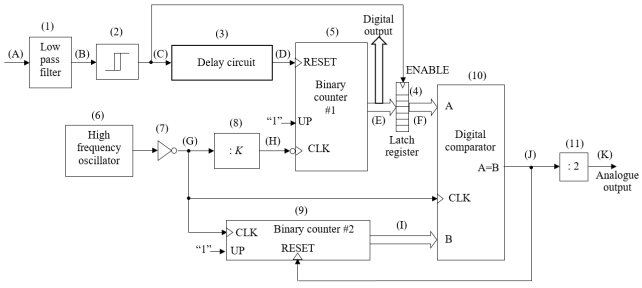

Figure 3. A detailed realization of the frequency extraction and multiplication circuit described in [14].

The idea behind this solution is to use frequency dividers based on binary counters to achieve multiplication. The input signal $x(t)$ with an unknown or varying fundamental frequency f0 is brought to input (A). The core of the circuit is an ultra-high frequency oscillator (6) with a base frequency $f_{ref.}$ The circuit divides this high frequency with a custom number K, which represents the desired fixed number of samples to be taken within each signal period $T = 1/ (f_0 \pm \Delta f)$. So we want the analogue output of the circuit to be used as a digital clock with the period equal to:

$$T_K = \frac{T}{K} \pm \frac{1}{2f_{ref}} = \frac{1}{(f_0 \pm \Delta f)K} \pm \frac{1}{2f_{ref}} \quad (1)$$

The circuit first divides the reference frequency f_{ref} with K to obtain the clock input for the up counter (5) and then counts the actual number of samples that can be taken with such frequency. The resulting number (E) in a digital format is used as a primary digital output of the circuit to provide insight into the actual fundamental frequency f_0 for further interpretation of the signal processing results, as will be explained later. Simultaneously the f_{ref} is fed to a binary counter (9) to provide the high digital number corresponding to the rate of the reference clock. Digital comparator (10) is then used to reset the high-speed binary counter (9) whenever K is reached. This creates a digital signal depicted in Fig. 4.

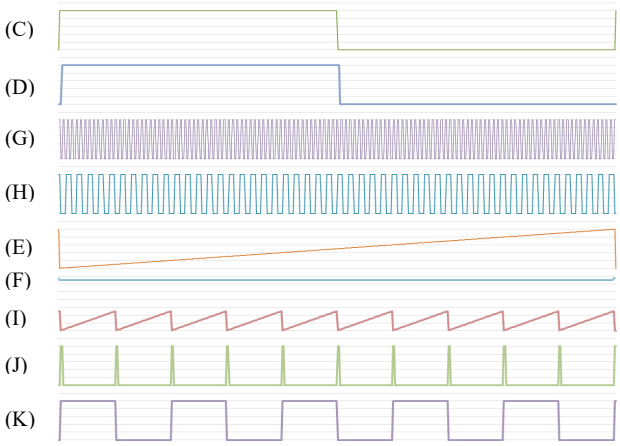

Figure 4. Illustration of all signals (C) to (K) from the schematics in Fig. 3 for a fixed value of parameter K.

The final divider with the factor 2 is introduced to stabilize clock signal, set its duty cycle to 50%, but also to compensate the fact that the counter (5) only counts during one half of the period of the input signal and will be reset afterwards.

The results obtained by any form of Fourier's transform from properly sampled input signal, will result in the spectrum shown in Fig. 5.

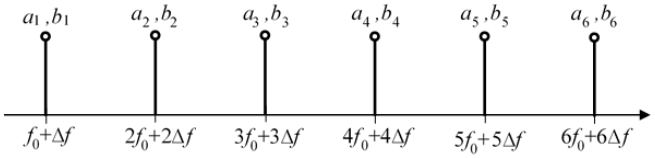

Figure 5. Correct spectrum without overlaping, leaking or phantom components regardless of the unkown value of the frequency drift Δf.

Obviously, the higher the reference frequency f_{ref} the smaller is the error that will be made. The higher the demand for the number of samples, the higher frequency f_{ref} has to be considered. Nevertheless, the proposed circuit provides a very good solution that can be realized with rather simple and low-cost hardware. So simple that it can be considered either as a separate circuit, or as an integral part of a larger VLSI chip. These two possible means of integration will be considered, which can be implemented straightforwardly in various hybrid electronic architectures.

The final step in spectrum reconstruction is to assign values to frequencies at the f-axis in Fig. 5, where true energies are located. For this, it is necessary to consider the digital output (E) of the binary counter (5) where the actual value of the division factor of f_{ref} to the unknown value of f_0 with resolution equal to the half of the interval of f_{ref}.

$$N_E = \frac{f_{ref}}{K(f_0 \pm \Delta f)} \pm \frac{1}{2} \quad (2)$$

Since f_{ref} is known, K is selected by the designer and N_E is provided by the circuit in a digital form, one can obtain $f_0 \pm \Delta f$ as

$$f_0 \pm \Delta f = \frac{f_{ref}}{K(N_E \pm \frac{1}{2})} \quad (3)$$

With each signal period, the value of $f_0 \pm \Delta f$ may be different, but the spectrum provided with Fig. 5 will remain correct. However, its way of displaying may need to be updated each time Δf changes which can be observed through changes of N_E.

2.2 Architecture for Adaptive Sampling

The most obvious implementation of the proposed circuit is to implement it independently from the main clock of the VLSI and to use it only to drive the analogue-to-digital conversion. In this scenario, the circuit is connected only to the electronics close to analogue inputs and apart from the main VLSI clock (CLK2) that is used to run the digital part of the chip. This configuration is illustrated in Fig. 6.

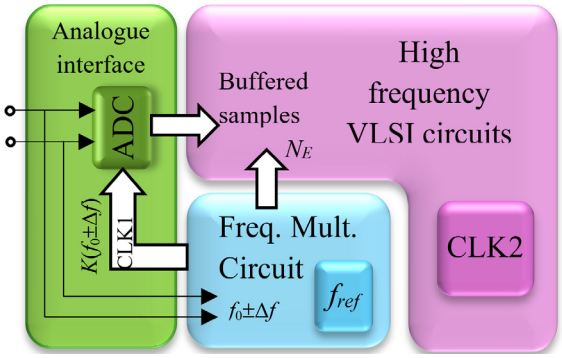

Figure 6. Using the frequency multiplication circuit only for the sampling of the input signal.

The frequency of the analogue input signal is multiplied with the programmed value of K (could be predetermined or customizable) and it is fed back to the ADC to enable exactly K samples to be taken within each period. In this configuration, there are several design strategies allowed, but they all require the samples from the ADC to be buffered or latched to compensate for the lack of synchronicity between the analogue and the digital portion of the circuit. This solution is easy to design and has been tested using discrete components, i.e. separate chips for the frequency multiplication device and separate for the main VLSI chip. One system on chip has been used to implement the drive for the signal sampling and another to implement signal processing. The practical realization is shown in Fig. 7.

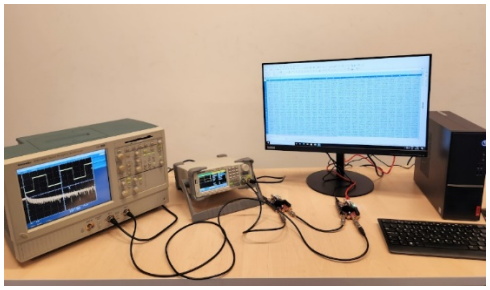

Figure 7. Implementation of the proposed achitecture for adaptive sampling

The results of its implementation have been illustrated in Fig. 7 and Table I. The signal that has been analyzed was a periodic rectangle with amplitude 10 V_{pp} and fundamental frequency varied from 37 Hz to 167 Hz using a 0.5 Hz step, generated with a digital signal generator. Frequencies of 50 Hz and 100 Hz have been skipped to avoid interferences and modulations from the power supply network. The output was displayed on a computer screen since the systems on the chip do not have their own native graphic displays. Constant displacement error and small deviations in amplitude values confirm the validity of straightforward implementation of the FFT, without any pre-filtering of spectrum post-processing.

Table 1. Deviations for the first 20 spectral components

Harmonic order	Spectrum distortion after applying FFT		Harmonic order	Spectrum distortion after applying FFT	
	Position deviation (mHz)	*Amplitude deviation* (mV)		*Position deviation* (mHz)	*Amplitude deviation* (mV)
1	±0.001	±0.02	11	±0.001	±0.05
2	±0.003	±0.03	12	±0.002	±0.08
3	±0.002	±0.01	13	±0.001	±0.30
4	±0.001	±0.05	14	±0.003	±0.20
5	±0.003	±0.03	15	±0.002	±0.60
6	±0.002	±0.06	16	±0.001	±0.80
7	±0.001	±0.07	17	±0.003	±0.40
8	±0.002	±0.02	18	±0.003	±0.50
9	±0.003	±0.03	19	±0.001	±0.90
10	±0.001	±0.04	20	±0.002	±0.70

3 Conclusion

The functionality of the proposed Frequency Multiplication Circuit has been tested against the desired clock rate of the instrument. A scenario for its implementation in high speed digital circuits with separate asynchronous analogue add-on has been investigated. The experiment conducted for this scenario confirmed the validity of the concept. It demonstrated with sufficient accuracy the consistency of the spectral image and the absence of any spectral leakage. The proposed approach to clocking allows the reminder of the instrument to be designed and utilized more efficiently by lowering the demands for computational resources.

4 References

[1] Li A., Yao C., Xia J., et al., 'Advances in cost-effective integrated spectrometers', Light: Science & Applications (11), 2022, pp 174, doi: 10.1038/s41377-022-00853-1.

[2] Goh Y., Jung D., Hwang G. and Chung J. -M., 'Consumer Electronics Product Manufacturing Time Reduction and Optimization Using AI-Based PCB and VLSI Circuit Designing', IEEE Transactions on Consumer Electronics, vol. 69, (3), pp. 240-249, Aug. 2023, doi: 10.1109/TCE.2023.3240249.

[3] Harika B., Sharath Kumar D.R.V.A., Kavya K., 'Revolutionizing the Future: Exploring the Potential of Low Power VLSI Technologies', Journal of Basic Science And Engineering, Vol. 21, (1) 2024, ISSN: 1005-0930, pp 1762-1771, https://www.researchgate.net/publication/389101396.

[4] Mandache L., L. and Al-Haddad K., 'New high precision harmonic analysis method for power quality assessment', Canadian Conference on Electrical and Computer Engineering 2005, 1-4 May 2005, Saskatoon, Saskatchewan, Canada, pp. 1958-1961, doi: 10.1109/CCECE.2005.1557366.

[5] Szmajda M., Gorecki K. and Mroczka J., 'DFT algorithm analysis in low-cost power quality measurement systems based on a DSP processor', 2007 9th International Conference on Electrical Power Quality and Utilisation, Barcelona, Spain, 2007, pp. 1-6, doi: 10.1109/EPQU.2007.4424081.

[6] Xanthopoulos T, 'Clocking in Modern VLSI Systems', Integrated Circuits and Systems, Springer, ISBN 978-1-4419-0260-3, 2009, doi:10.1007/978-1-4419-0261-0.

[7] Moo C. S., Chang Y. N. and Mok P. P., 'A digital measurement scheme for time-varying transient harmonics', IEEE Transactions on Power Delivery, Vol. 10, (2), pp. 588-594, April 1995, doi: 10.1109/61.400874.

[8] Karimi-Ghartemani M. and Iravani M. R., 'Measurement of harmonics/inter-harmonics of time-varying frequencies', IEEE Transactions on Power Delivery, Vol. 20, (1), pp. 23-31, Jan. 2005, doi: 10.1109/TPWRD.2004.837674.

[9] Antić B. M., Mitrović Z. L., Vujičić V. V., 'A Method for Harmonic Measurement of Real Power Grid Signals with Frequency Drift using Instruments with Internally Generated Reference Frequency', Measurement Science Review, Volume 12, (6), 2012, pp. 277-285, doi: 10.2478/v10048-012-0038-1.

[10] Lara-Reyes J., Ponce-Silva M., Hernández-González L. at all., 'Series RLC Resonant Circuit Used as Frequency Multiplier', Energies 2022, (15), 2024, pp. 9334. doi: 10.3390/en15249334.

[11] Rai R. K. and Lohchaab N., 'Higher Order Harmonic Generation Using Capacitive Nonlinearity of the Step Recovery Diode', 2023 IEEE Microwaves, Antennas, and Propagation Conference (MAPCON), Ahmedabad, India, 2023, pp. 1-4, doi: 10.1109/MAPCON58678.2023.10463836.

[12] Haraoubia B., 'Non-Linear Electronics 2: Chapter 3 The Phase Locked Loop (PLL): 3.9.2 Frequency Synthesis', T2019, ISBN 978-1-78548-301-1, ISTE Press - Elsevier 2019, pp 205-208. doi: 10.1016/C2019-0-02486-7.

[13] B. J. Kaczynski, 'Digital signal processing employing a clock frequency which is always a constant integer multiple of the fundamental frequency of an input analog signal', US patent US20080232526A1, 2007.

[14] B. Santrac, B. Antic, 'Frequency multiplying device', EU patent, EP17000650.6A, 2017.

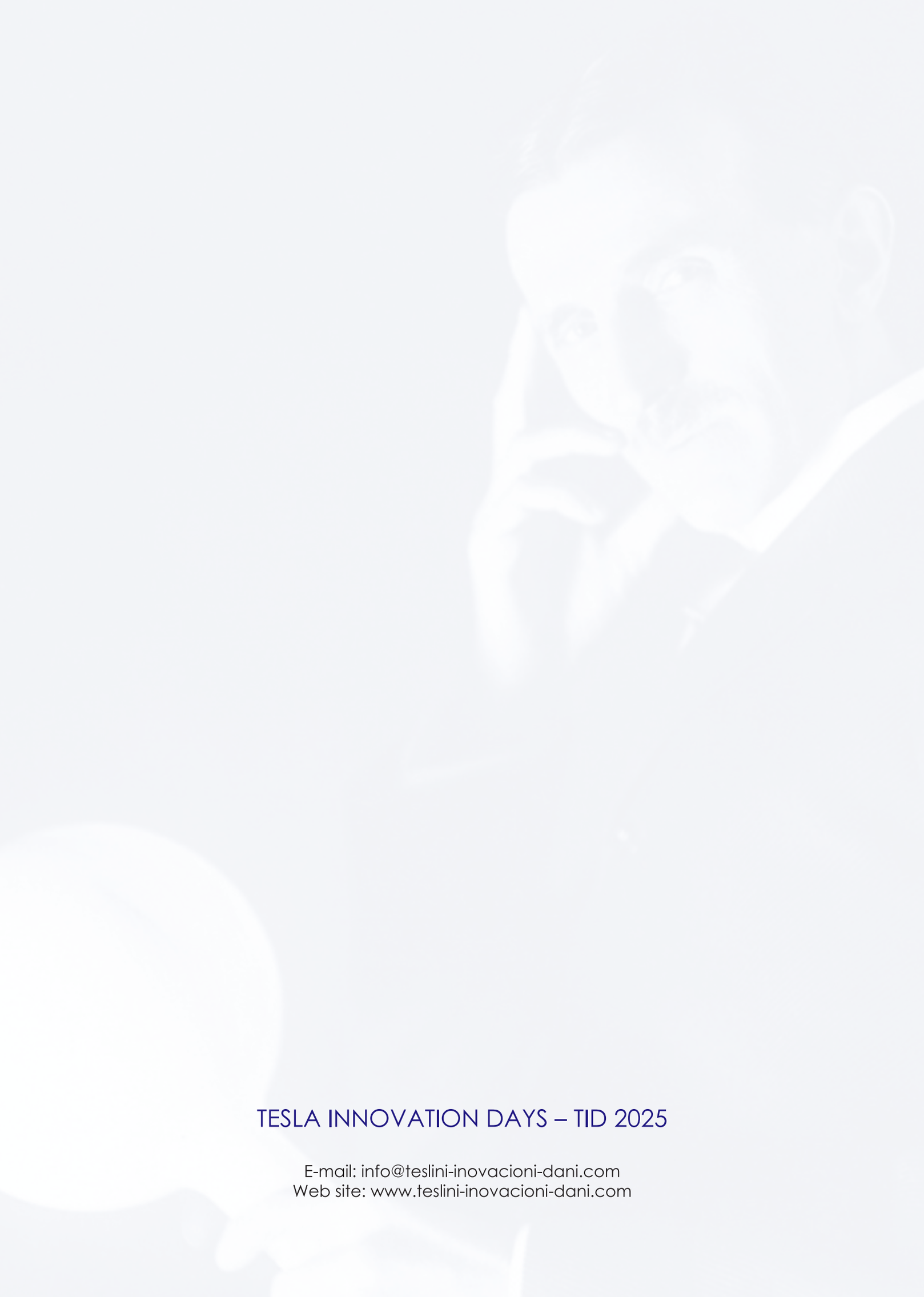

TESLA INNOVATION DAYS – TID 2025

E-mail: info@teslini-inovacioni-dani.com
Web site: www.teslini-inovacioni-dani.com

ТЕСЛИНИ ИНОВАЦИОНИ ДАНИ

TESLA INNOVATION DAYS

Belgrade, Serbia, April 7 - 8, 2025